Combustion and Flame 160 (2013) 366–383

Contents lists available at SciVerse ScienceDirect

Combustion and Flame

journal homepage: www.elsevier.com/locate/combustflame

Inert-droplet and combustion effects on turbulence in a diluted diffusion flame

Jun Xia [a,b,*], Hua Zhao [a], Athanasios Megaritis [a], Kai H. Luo [b,c], Alasdair Cairns [a], Lionel C. Ganippa [a]

[a] Mechanical Engineering Subject Area & Centre for Advanced Powertrain and Fuels, School of Engineering and Design, Brunel University, Uxbridge UB8 3PH, UK
[b] Energy Technology Research Group, Faculty of Engineering and the Environment, University of Southampton, Southampton SO17 1BJ, UK
[c] Centre for Combustion Energy, Key Laboratory for Thermal Science and Power Engineering of Ministry of Education, Department of Thermal Engineering, Tsinghua University, Beijing 100084, China

ARTICLE INFO

Article history:
Received 5 May 2012
Received in revised form 7 September 2012
Accepted 7 October 2012
Available online 1 November 2012

Keywords:
DNS
Diffusion flame
Reacting mixing layer
Droplets
Evaporation
Turbulence kinetic energy

ABSTRACT

The inert-droplet and combustion effects on turbulence in a diluted diffusion flame are investigated using direct numerical simulation (DNS) through parametric study. The computational configuration is a temporally-developing reacting mixing layer laden with close to 17×10^6 inert evaporating droplets. The gas phase is described in the Eulerian frame while the discrete droplet phase is traced in the Lagrangian frame, with strong two-way coupling between the two phases through mass, momentum, and energy exchange. In the two-way coupling, distributing droplet source terms onto the Eulerian grids is a key procedure. Different distribution methods are compared to examine its impact on the statistics, including correlations between droplet source term and gas phase flow variables. The physical parameter considered is the characteristic droplet evaporation time, which is varied with the latent heat of vapourisation and plays a crucial role in both dynamic and evaporation effects of droplets on the turbulent reacting flow. To detail the analysis, the transport equation for the turbulence kinetic energy (TKE) is employed, in which the droplet contributions are categorised into three terms. The direct droplet and combustion effects on the TKE and their effects on the turbulence production and dissipation rate, pressure-dilatation are then scrutinised and compared to analyse the interactions among turbulence, combustion, and inert droplets in the multi-phase reacting flow.

1. Introduction

Turbulent multi-phase combustion remains an important and unresolved subject in combustion science as one of the most challenging fundamental and practical problems. First, energy conversion is usually related to the transfer of chemical energy to sensible energy via combustion in a turbulent flow, which is often further complicated by a dispersed phase such as solid fuel particles or liquid fuel spray droplets. For instance, liquid fuel injection is one of the most common procedures in non-premixed combustion systems such as internal combustion engines and aircraft gas turbine combustors for road and air transportation. Another important practical application is pulverised-coal combustion in coal-fired power stations.

Another type of turbulent multi-phase reacting flow is non-premixed gas combustion diluted with or suppressed by inert evaporating droplets. It appears in a multiplicity of industrial and residential applications such as the water-misting, dilution or injection technique [1–3] and combustion suppression using water sprays/mists [4–6], and is thus practically important and scientifically interesting. Compared to the concentrated interest in solid- and liquid-fuel-based combustion, publications on turbulent multi-phase combustion of this kind are relatively few, despite its crucial role in the water-injection technique and fire safety engineering. Due to the distinct role played by the inert droplets, the combustion physics is completely different from that in spray combustion with entirely new classes of phenomena. Therefore, to properly model the multi-phase reacting flow, we must improve the scientific understanding on the complex multilateral unsteady, nonlinear interactions among turbulence, combustion, and droplets.

Over the past several decades, study using high-fidelity numerical techniques on the interaction between combustion and turbulence [7] has been active for both premixed [8–10] and non-premixed [11–13] flames. The turbulent burning velocity [14] is a typical and important research topic in studying the complex interactions of turbulence and premixed combustion. The relationship between turbulent scalar flux and local dilatation in premixed flames were investigated in [15] using two-dimensional DNS databases involving a multi-step chemical mechanism. In [16], zone conditional averaging [17] was applied to the DNS database of a turbulent premixed flame to understand the mechanism of flame-generated turbulence. The effects of Lewis

* Corresponding author at: Mechanical Engineering Subject Area & Centre for Advanced Powertrain and Fuels, School of Engineering and Design, Brunel University, Uxbridge UB8 3PH, UK. Fax: +44 1895 256 392.
E-mail address: jun.xia@brunel.ac.uk (J. Xia).

0010-2180
http://dx.doi.org/10.1016/j.combustflame.2012.10.007

number, i.e., differential diffusion rates of heat and mass, on turbulence kinetic energy transport in premixed flames were investigated using DNS database in [18]. For non-premixed combustion, the effect of combustion-released heat on turbulence has been scrutinised based on budget analysis of the transport equation of turbulence kinetic energy using DNS in temporally-developing mixing layer [19,20], spatially-developing mixing layer [21], and homogeneous shear turbulence [22].

In parallel to the research on interaction between combustion and turbulence, interaction between solid particles, liquid droplets and turbulent flow has also received considerable research interest due to the ubiquitous phenomenon of gas-solid and gas-liquid two-phase turbulent flow in engineering combustion devices and applications. The current state of the research on turbulent dispersed multi-phase flow was recently reviewed in [23], with mechanisms of turbulence modulation due to particles as one of the main themes.

The preferential concentration [24–26] of particles is a key feature of particle distribution in turbulent flow and determined by the ratio of the inertia between the two phases, which is quantified by the Stokes number St. For the $St \sim 1$ particles, the preferential concentration is most manifest, i.e., particles accumulating in high-strain-rate regions and avoiding high-vorticity regions. In liquid-droplet-laden turbulent flows, the preferential concentration has important implication on droplet evaporation and turbulent scalar mixing. As shown in [27], the preferential segregation of droplets in homogeneous isotropic turbulence is important for the evolution of global variables such as the mean mixture fraction $\overline{Z}$ and mixture fraction fluctuations Z', which are the key parameters of non-premixed combustion models. In a DNS study of reacting droplets interacting homogeneous shear turbulence [28], the reaction rate is found higher in high-strain-rate regions due to the preferential concentration of fuel droplets in those regions.

Due to its capability of resolving the large-scale motion of the turbulence, the LES methodology for engineering multi-phase flows has been under active development with the rapid advance of computational techniques. LES of swirling particle-laden flows in a coaxial-jet combustor was performed in [29], where the filtered incompressible Navier–Stokes equations were solved and efficient particle-tracking scheme was developed on unstructured grids for the complex engineering configuration. In [30], the probabilistic approach [31] was developed for the dispersed phase. It is based on the transport equation for the spatially filtered joint probability density function of a set of macroscopic particle variables. The approach was extended in [32] to incorporate a stochastic subgrid model of particle breakup to simulate spray atomisation using LES.

Compared to the research on the bilateral turbulence–combustion and turbulence–particles/droplets interactions, publications on the multilateral turbulence–combustion–particles/droplets interactions are relatively few. In [28], evaporation and combustion of fuel droplets dispersed in a compressible oxidiser gas were investigated using DNS in homogeneous shear turbulence. The particle effects on turbulence and diffusion of reactive species were studied using DNS in a spatially-developing particle-laden turbulent mixing layer with an isothermal chemical reaction in [33]. DNS was used for fundamental studies of the ignition of two-dimensional temporally-developing fuel spray jets with detailed chemical mechanism incorporated in [34]. LES of spray–turbulence–flame interactions in a lean direct-injection combustor was performed in [35]. A spray breakup model was employed to eliminate the need to specify the inflow conditions of the liquid phase, i.e., droplet sizes and velocities. In [36], ignition and the subsequent turbulent edge spray flame propagation in fuel-droplet-laden turbulent mixing layers were studied using DNS.

As can be seen, the complex interactions among the hydrodynamic turbulence, combustion and a dispersed phase are further compounded by new physical phenomena if a liquid phase is engaged. Among others, evaporation is another key phenomenon which must be prudently considered to fully account for the interactions between the two phases. In addition to all the physical effects (preferential concentration and turbulence modulation) of solid particles due to the interphase aerodynamic drag, which leads to momentum exchange between the phases and governs particle effects on the turbulent flow, evaporation also causes both mass and thermal energy exchange between the gas and liquid phases. For a non-premixed gaseous flame diluted with inert droplets, mass addition by the third scalar-inert evaporated vapour, which is neither the fuel gas nor the oxidiser gas, leads to the breakdown of mass conservation in the control system of the gas phase. Therefore the conventional mixture fraction cannot be directly applied and a new mixture fraction has been proposed for the system of non-premixed gas combustion diluted with inert droplets [37]. Compared to the heat transfer due to temperature difference between solid particles and the carrier phase, the heat exchange to provide the latent heat of vapourisation for droplet evaporation could be significant. Meanwhile evaporation causes the decrease of droplet size and droplets vanish when evaporation completes, which will alter droplet distribution in and thus droplet dynamic effects on the flow. Combustion-released heat has been known as an important mechanism of combustion effect on turbulence [20–22]. Dispersed in the reacting flow, droplets absorb combustion-released heat to drive evaporation. Therefore the combustion effects on turbulence will be affected by droplet evaporation.

Similar to the particle dynamic response time τ_d which is a characteristic time scale designating how rapidly particles respond to flow dynamics, droplet evaporation can be characterised by the droplet life time or characteristic evaporation time τ_v, which can significantly affect the droplet effects, due to both droplet dynamics and evaporation, on turbulence and consequently the turbulence–combustion–droplets interactions. The topic of the effects induced by droplet evaporation on the turbulence–combustion–droplets interactions has not been sufficiently investigated and will be the main objective of the present study.

Specifically, the objective of this paper is to investigate the inert-droplet effects, including droplet evaporation and momentum exchange with the carrier phase via the interphase drag, and combustion effects on flow turbulence. A temporal turbulent reacting mixing layer initially laden with close to 17×10^6 inert droplets is simulated, with the characteristic evaporation time scale τ_v as the key parameter in the parametric study. The transport equation of the turbulence kinetic energy is employed to detail the analysis, in which the droplet effects have been classified in three terms, i.e., the power due to the interphase drag, the power due to an "evaporating drag", and an additional production rate due to evaporation. By integrating the TKE transport equation across the mixing layer, the redistributive terms which transport, but do not produce or dissipate, TKE within the flow disappear, and the droplet and combustion effects on the TKE and their effects on the turbulence production and dissipation rate, pressure-dilatation are then scrutinised and compared to analyse the interactions among turbulence, combustion and inert evaporating droplets in the multi-phase reacting flow.

To achieve the objective, DNS has been used to numerically solve the turbulent flow field. Due to the manifest rapid advances of computational power and numerical algorithms over the past two decades, a wealth of information, for example high-order correlations between fluctuating quantities, can now be obtained via high-fidelity numerical simulations and is otherwise unavailable [38]. In particular, DNS has become a powerful tool to explore

the complex physics in combustion-related phenomena where unsteadiness and nonlinearity occur at disparate temporal and spatial scales. DNS has also been used to develop, validate, and calibrate advanced engineering models for RANS (Reynolds-Averaged Navier–Stokes) and LES (Large-Eddy Simulation), where averaging techniques have been used to limit the dynamic range of scales and to obtain the solutions of model equations. Detailed information must be obtained to develop closures for the unknown terms generated due to the averaging of nonlinear terms in these equations, for which DNS is an ideal tool.

Still, since DNS requires a full numerical solution be obtained from the smallest to the largest of the characteristic scales, DNS of the instantaneous governing equations can be attempted only in limited cases. In the present study, the simulations fully resolve the carrier-phase flow down to the Kolmogorov scale. To resolve the flow inside and around the droplets in a many-droplet turbulent reacting flow is, however, still far beyond the capacity of currently available supercomputers. The droplets are thus assumed as point sources and tracked in the Lagrangian frame as in most of the published DNS research on turbulent two-phase flows, whereas the unsteady compressible Navier–Stokes equations used for the gas phase are solved in the Eulerian frame. The two-way coupling between the Eulerian gas phase and the Lagrangian droplet phase, i.e., obtaining gas variables at the droplet location and projecting droplet source terms onto the Eulerian grids, in the hybrid Eulerian–Lagrangian approach entail additional limitations to the DNS. Moreover, a dilute fluid-droplet two-phase flow is simulated, where the droplet motion is primarily controlled by the surface force (interphase drag) and droplet–droplet collisions or interactions are not considered [39]. Due to the consideration of computational cost, chemical kinetics is also simplified to an idealised one-step global finite-rate irreversible chemical reaction. A temporal reacting mixing layer laden with inert droplets has been chosen as the computational configuration due to its important prototype value for engineering flow. Meanwhile DNS is tractable for the simplified yet realistic realisation where complex turbulence–combustion–droplets interactions occur.

The DNS/LES code **MultiPLESTaR** (**Multi-P**hase **L**arge-**E**ddy **S**imulation of **T**urbulence a**n**d **R**eaction) was used to perform the simulations. The code has been used in a series of DNS/LES studies on turbulent multi-phase reacting flows [6,37,40–43]. In [41], grid independence study was performed and excellent agreement of the statistics was achieved between the cases with different grid numbers in DNS of inert-droplet-laden temporal reacting mixing layers.

2. Mathematical formulations and numerical procedures

The fluid dynamics of the gas phase is modelled by the compressible unsteady Navier–Stokes equations. The transport equations for the fuel gas, oxidiser gas, and evaporated vapour are used to trace the reactive and inert gas species. The non-dimensional governing equations for the gas phase are as follows:

$$\frac{\partial \rho_g}{\partial t}+\frac{\partial(\rho_g u_{g,i})}{\partial x_i}=S_{ms}, \tag{1}$$

$$\frac{\partial(\rho_g u_{g,i})}{\partial t}+\frac{\partial}{\partial x_j}(\rho_g u_{g,i}u_{g,j}+p\delta_{ij}-\sigma_{ij})=S_{mo,i}, \tag{2}$$

$$\frac{\partial E_T}{\partial t}+\frac{\partial}{\partial x_i}[(E_T+p)u_{g,i}+q_i-u_{g,j}\sigma_{ij}]=Q_m\dot{\omega}_T+S_{en}, \tag{3}$$

$$\frac{\partial(\rho_g Y_n)}{\partial t}+\frac{\partial}{\partial x_i}\left(\rho_g Y_n u_{g,i}-\rho_g\mathcal{D}\frac{\partial Y_n}{\partial x_i}\right)=-\upsilon_n W_n\dot{\omega}_T, \tag{4}$$

$$\frac{\partial(\rho_g Y_v)}{\partial t}+\frac{\partial}{\partial x_i}\left(\rho_g Y_v u_{g,i}-\rho_g\mathcal{D}\frac{\partial Y_v}{\partial x_i}\right)=S_{ms}. \tag{5}$$

In the equations, the subscripts "g" and "d" illustrate a gas or droplet variable. The symbol "*n*" stands for fuel "f" or oxidiser "o", "v" for evaporated vapour. ρ, u, and Y denote density, gas velocity, and species mass fraction, respectively. E_T is the total energy per unit volume of the gas phase, $E_T=\rho_g(e_g+u_{g,i}u_{g,i}/2)$, where e_g is the internal energy per unit mass of the gas phase, $e_g=T_g/[\gamma(\gamma-1)Ma^2]+Y_v h_{v,0}$. $h_{v,0}$ is the reference enthalpy for the vapour. S_{ms}, $S_{mo,i}$, and S_{en} are droplet source terms and will be discussed later. σ_{ij} is the viscous stress tensor, $\sigma_{ij}=2\mu/Re(S_{ij}-\delta_{ij}/3S_{kk})$, where μ is the molecular viscosity of the gas phase and S_{ij} the strain rate tensor, $S_{ij}=0.5(\partial u_{g,i}/\partial x_j+\partial u_{g,j}/\partial x_i)$. The heat conduction flux is $q_i=-\mu/[(\gamma-1)Ma^2 Pr\ Re]\partial T_g/\partial x_i$. υ, W, and Q_m are the stoichiometric coefficient of the reaction, molecular mass, and combustion-released heat [20], respectively. The mass diffusion coefficient $\mathcal{D}$ is given by $\mathcal{D}=\mu/(\rho_g ReSc)$. The gas pressure p, temperature T_g, and density ρ_g are correlated by the ideal gas law. γ, *Re*, *Ma*, *Sc*, and *Pr* are the ratio of specific heats, the Reynolds number, Mach number, Schmidt number, and Prandtl number, respectively. The Prandtl and Schmidt numbers are both assumed to be constant, i.e., $Pr=Sc=0.697$.

The reaction rate $\dot{\omega}_T$ is modelled by the Arrhenius law for a global one-step finite-rate irreversible chemical reaction,

$$\dot{\omega}_T=Da\left(\frac{\rho_g Y_f}{W_f}\right)^{\upsilon_f}\left(\frac{\rho_g Y_o}{W_o}\right)^{\upsilon_o}\exp\left(-\frac{Ze}{T_g}\right), \tag{6}$$

where *Da* and *Ze* are the Damköhler and Zel'dovich numbers, respectively.

All the variables and quantities presented in this paper have been non-dimensionalised using the following reference quantities: (1) the initial density of the oxidiser stream $\rho_r^*=\rho_{O,0}^*$, (2) the velocity difference between the fuel and oxidiser stream $u_r^*=\Delta U_0^*=2U_0^*$, (3) $p_r^*=\rho_r^* u_r^{*2}$, (4) the initial vorticity thickness of the mixing layer $l_r^*=\delta_{\omega,0}^*$, (5) $t_r^*=l_r^*/u_r^*$, (6) the initial temperature of the oxidiser stream $T_r^*=T_{O,0}^*$, and (7) $e_r^*=h_r^*=u_r^{*2}$. The superscript "*" designates a dimensional variable.

As shown by Eqs. (4) and (5), in the present study the fuel and oxidiser are both in gas phase and have reaction but no evaporation source terms in their transport equations, while the transport equation of vapour has evaporation but no reaction source terms. The system is different from spray combustion and characterises gas combustion diluted with or suppressed by inert droplets.

Droplets are traced in the Lagrangian framework as point sources in the flow field and have their own governing equations for mass, momentum and energy, which can be written as

$$\dot{m}_d\equiv\frac{dm_d}{dt}=-\frac{1}{3}\frac{Sh}{Sc}\frac{m_d}{St}H_M, \tag{7}$$

$$\frac{dv_{d,i}}{dt}=\frac{F_{drag,i}}{m_d}=\frac{f}{St}(u_{g,i}-v_{d,i}), \tag{8}$$

$$\frac{dT_d}{dt}=\frac{1}{3St}\left[\frac{Nu}{Pr}(T_g-T_d)-(\gamma-1)Ma^2\frac{Sh}{Sc}H_M h_{fg}\right], \tag{9}$$

where m_d and $\vec{v}_d$ are the droplet mass and velocity. The Stokes number *St* is defined as the ratio of the droplet dynamic response time scale to a characteristic large-scale flow time scale, i.e.,

$$St=\frac{\tau_d^*}{\tau_g^*}=\frac{\rho_d D_d^2}{18\mu/Re}, \tag{10}$$

where D_d is droplet diameter. It is known that the gas transport property μ is a function of gas temperature and thus affected by combustion-released heat. In the present study the dynamic viscosity μ is set to be a constant 1 . Consequently, the Sotkes number *St* solely depends on the droplet diameter D_d and the indication of droplet inertia by the Stokes number is recovered.

The Sherwood and Nusselt number is denoted as Sh and Nu, respectively, $Sh = 2 + 0.552Re_d^{1/2}Sc^{1/3}$ and $Nu = 2 + 0.552Re_d^{1/2}Pr^{1/3}$. The droplet Reynolds number Re_d is defined as $Re_d = Re\rho_g|\vec{u}_g - \vec{v}_d|D_d/\mu$. The specific driving potential for mass transfer H_M is defined as $H_M = \ln(1 + B_M)$, where the equilibrium Spalding transfer number for mass B_M is $B_M = (Y_{s,eq} - Y_{v,far})/(1 - Y_{s,eq})$. The vapour mass fraction at far field $Y_{v,far}$ is approximated by Y_v at the droplet location. The vapour mass fraction at the droplet surface $Y_{s,eq}$ is obtained from its molar fraction $\chi_{s,eq}$ at the droplet surface, $Y_{s,eq} = \chi_{s,eq}/[\chi_{s,eq} + (1 - \chi_{s,eq})W_g/W_v]$. $\chi_{s,eq} = p_{sat}/p$, where the saturation pressure p_{sat} is determined by the Clausius–Clapeyron law, $p_{sat} = p_{atm}\exp[\gamma Ma^2 W_v h_{fg}(1/T_B - 1/T_d)]$. p_{atm} is atmospheric pressure, and T_B the normal boiling temperature or the saturation temperature at p_{atm}. $\vec{F}_{drag}$ is the drag force exerted on droplets by the turbulent reacting flow, and h_{fg} the latent heat of vapourisation. f is a correction coefficient to Stokes drag, $f = 1 + 0.15Re_d^{0.687}$.

The droplet effects on the flow field are modelled by the droplet source terms shown in Eqs. (1)–(3), (5), which can be written as

$$S_{ms} = -\frac{1}{V}\sum_k \dot{m}_{d,k}, \tag{11}$$

$$S_{mo,i} = -\frac{1}{V}\sum_k (F_{drag,k,i} + \dot{m}_{d,k}v_{d,k,i}), \tag{12}$$

$$S_{en} = -\frac{1}{V}\sum_k \left[\frac{1}{3}\frac{Nu_k}{(\gamma-1)Ma^2Pr}\frac{m_{d,k}}{St_k}(T_{g,k} - T_{d,k}) + \frac{1}{(\gamma-1)Ma^2}\dot{m}_{d,k}T_{d,k} + \dot{m}_{d,k}h_{fg} + F_{drag,k,i}v_{d,k,i} + \frac{1}{2}\dot{m}_{d,k}v_{d,k,i}v_{d,k,i}\right], \tag{13}$$

where V is the local volume surrounding a grid point and k the kth droplet in that volume.

The schematic diagram of the computational configuration, a temporally-developing inert-droplet-laden reacting mixing layer, is depicted in Fig. 1. As shown, the fuel and oxidiser streams are the upper and lower streams, respectively, and move in opposite directions with equal streamwise speed U_0 [43]. The letters x, y, z or subscript numbers 1, 2, 3 refer to the streamwise, cross-stream and spanwise directions, respectively. The initial laminar mixing layer is excited by strong spanwise and streamwise vorticity perturbations [43,44]. The computational domain lengths in both the streamwise and spanwise directions equal four disturbance wavelengths, i.e., $L_x = 4\lambda_x$ and $L_z = 4\lambda_z$, where $\lambda_z = 0.6\lambda_x$ and $\lambda_x = 1.16(2\pi)\delta_{\omega,0}$. By setting $L_y = 2L_x$, the cross-stream domain size is large enough to have minimal influence on the main interaction region of the inert-droplet-laden reacting mixing layer. At $t_0 = 225$, a fully turbulent mixing layer is reached after the roll-up, pairing, second pairing and transition stages. At $t = t_0$, reaction is enabled in the droplet-free reacting mixing layer case; for the droplet-laden counterpart cases, the droplet effect on the flow is disabled before $t = t_0$ by setting $S_{ms} = S_{mo,i} = S_{en} = 0$. The droplets are therefore "flow tracer particles" until $t = t_0$. Thereafter, both reaction and droplet effects are enabled. Compared to the widely used configuration of droplet-laden homogeneous isotropic or shear turbulence in which a synthetic energy spectrum is used to provide the initial condition of turbulence, the current computational configuration is more close to the scenario in realistic combustion systems, for which DNS is tractable. Spray breakup and atomisation is not simulated. The focus of the present study is to investigate the turbulence–combustion–droplets interactions in the dilute flow regime of a fluid-droplet mixture. For this purpose, the same initial condition of turbulence with identical droplet distribution is arranged for the parametric study of effects of combustion and inert droplets with distinct characteristic evaporation time scales on turbulence.

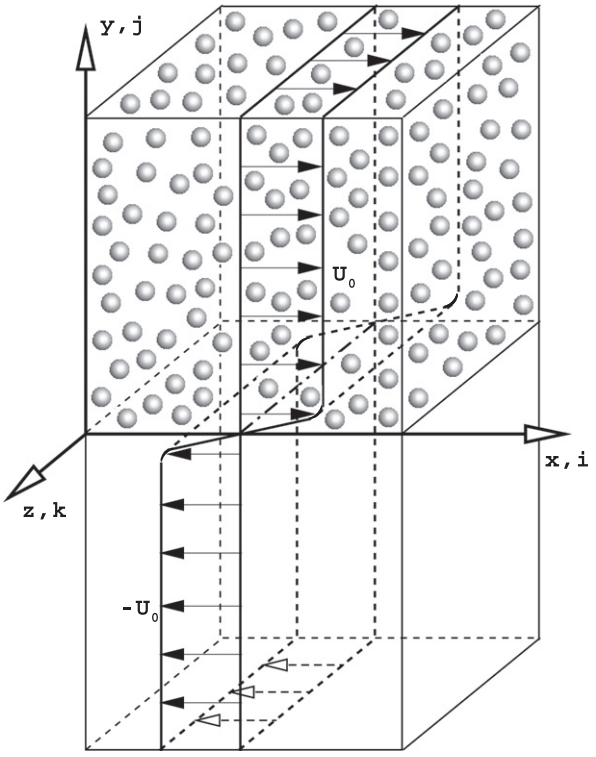

Fig. 1. Schematic of the inert-droplet-laden mixing layer. The fuel stream is in the upper half of the domain with randomly embedded inert droplets and moving in the positive x direction, while the oxidiser stream in the lower half moving in the negative x direction with the same velocity magnitude as that of the fuel stream U_0. The initial gas streamwise velocity $u_{g,x}$, initial fuel and oxidiser mass fraction Y_f and Y_o and initial droplet number density n_d are prescribed by an error function $erf[\pi^{1/2}y/\delta_{\omega,0})$, where $\delta_{\omega,0}$ is the initial vorticity thickness. The initial droplet velocity and temperature are identical to those of the carrier phase. The letters x, y and z denote the streamwise, cross-stream and spanwise directions, respectively. The streamwise x and spanwise z directions are periodic, and non-reflecting boundary conditions are applied at the cross-stream boundaries.

Error functions are prescribed for the initial profiles of the gas streamwise velocity $u_{g,1}$, mass fractions of fuel Y_f and oxidiser Y_o, and droplet number density n_d. The liquid droplets are initially randomly seeded in the fuel stream according to the specified number density profile, with initial droplet velocity $\vec{v}_{d,0}$ and temperature $T_{d,0}$ identical to the local gas velocity $\vec{u}_{g,0}$ and ambient temperature $T_{g,0}$, respectively.

For the initial laminar mixing layer, the Reynolds number Re is $Re = 1000$ and the convective Mach number $M_c = 0.5$. The combustion parameters: the Damköhler number $Da = 5$, Zel'dovich number $Ze = 3$, and heat release parameter $Q_m = 7.5$ were chosen to model a finite-rate diffusion flame without inclusion of radiation calculations. For the droplets, $St_0 = 1$ and $MLR_0 = 0.4$, where St_0 and MLR_0 denote the initial Stokes number of droplets, $St_0 = \rho_d D_{d,0}^2/(18\mu/Re)$, and initial mass loading ratio, $MLR_0 = N_{d,0}m_{d,0}/(\rho_{g,0}L_xL_yL_z/2)$ (ratio of the initial droplet mass to the mass of the carrier stream-fuel), respectively. The initial droplet number in the domain is $N_{d,0} = 16{,}925{,}496$. The droplet density is $\rho_d = 827.8$, which is non-dimensionalised according to the density of water droplets.

As stated, droplet evaporation is dictated by the Clausius–Clapeyron law in the present study. To obtain different characteristic vapourisation time τ_v, the latent heat of vapourisation h_{fg} is varied, as shown in Table 1. In the meantime the normal boiling temperature T_B is kept the same as that of water. In Table 1, $h_\infty = H_{WV}$ corresponds to the latent heat of vapourisation of water at normal atmospheric conditions. The other h_{fg}, $h_0 = H_{WV}/10$, was chosen to perform parametric studies of the evaporation effect of inert

Table 1
Simulation parameters. H_{WV} is the latent heat of vaporisation of water at normal atmospheric conditions. τ_v is the characteristic vaporisation time of a droplet estimated with the initial condition. τ_t is the turbulent-eddy turn-over time estimated at $t = t_0$, when a fully turbulent mixing layer has been established. n_s designates the times of the application of the smoothing scheme to the droplet source terms S_{ms}, $\vec{S}_{mo}$, and S_{en} in every time step of DNS. The common parameters include: (1) *flow*: $Re = 1000$, $M_c = 0.5$, $Pr = Sc = 0.697$; (2) *combustion*: $Da = 5$, $Ze = 3$, $Q_m = 7.5$; (3) *droplets*: $St_0 = 1$, $\rho_d = 827.8$, $N_{d,0} = 16{,}925{,}496$. (4) *computational domain*: $L_x = 4\lambda_x$, $L_y = 2L_x$, $L_z = 4\lambda_z$, and $\lambda_x = 1.16(2\pi)\delta_{\omega,0}$, $\lambda_z = 0.6\lambda_x$; (5) *grid numbers*: $n_x \times n_y \times n_z = 384 \times 768 \times 232 = 68{,}419{,}584$.

Cases	h_{fg}	τ_v	n_s
RML	–	–	–
Dh_sn1	$h_0 = H_{WV}/10$	$\tau_{v,0} \ll \tau_t$	1
Dh_sn2	$h_0 = H_{WV}/10$	$\tau_{v,0} \ll \tau_t$	2
Dh_bn0	$h_\infty = H_{WV}$	$\tau_{v,\infty} \gg \tau_t$	0
Dh_bn1	$h_\infty = H_{WV}$	$\tau_{v,\infty} \gg \tau_t$	1

droplets on flow turbulence. If the initial condition is used for estimating τ_v, i.e., $\tau_v = 4.5ScSt_0/\ln(1 + B_M)$ [45], then $\tau_v \gg \tau_t$ for $h_\infty = H_{WV}$, and $\tau_v \ll \tau_t$ for $h_0 = H_{WV}/10$. τ_t is the turbulent-eddy turn-over time. It is approximated by $\tau_t = \bar{\rho}_g k/|\epsilon_k|$ at each homogeneous plane $x - z$ and the maximal value obtained in the range $-\delta_\omega/2 \leqslant y \leqslant \delta_\omega/2$ at $t = t_0$ is taken as τ_t. δ_ω is the vorticity thickness of the mixing layer. k denotes the Favre-mean turbulence kinetic energy and ϵ_k the turbulence dissipation rate (TDR), i.e., $k \equiv \widetilde{u''_{g,i}u''_{g,i}}/2$ and $\epsilon_k \equiv -\overline{\partial u''_{g,j}/\partial x_i \sigma_{ij}}$. The Favre mean $\tilde{f}$ and fluctuation f'' are defined as $\tilde{f} \equiv \overline{\rho_g f}/\bar{\rho}_g = \langle \rho_g f \rangle / \langle \rho_g \rangle$ and $f'' \equiv f - \tilde{f}$, respectively. A Reynolds-averaged variable is denoted as $\bar{f}$ or $\langle f \rangle$ and obtained in the present study via spatial averaging over homogeneous x–z planes.

Due to the hybrid Eulerian/Lagrangian system in which droplets are approximated as point sources, the two-way coupling between the two phases involves interpolating gas phase variables at the local droplet position and distributing the droplet source terms, S_{ms}, $\vec{S}_{mo}$, and S_{en} defined in Eqs. (11)–(13), onto the Eulerian grids. The former is achieved by a 4th-order Lagrange polynomial in the present study. While a high-order interpolation scheme such as Lagrange or Hermite can well achieve its purpose, the projection of droplet source terms onto Eulerian grids is more difficult in numerics. Currently there is no consensus on which method is most suitable. A common procedure is to add the source term of each individual droplet to its eight nearest neighbour grid points using a geometrical weighting [27,41,44]. Wang and Rutland [34] used a procedure which projects the source term farther than on the nearest nodes. In [41] where the current code in its earlier version was used, three different methods of droplet source term repartition were compared, and no systematic difference was found in the statistics. In the present study, the same smoothing scheme as in [44] is applied to the droplet source terms after they are allocated to the Eulerian grids using the above geometrically weighting method. The Eulerian source terms are then smoothed using a local procedure whereby the source at each individual grid node is shifted towards the average on the surrounding six nearest nodes with the smoothing coefficient C_s set to 0.75 [44], i.e.,

$$\widehat{S}_{i,j,k} = (1 - C_s)S_{i,j,k} + C_s S_{ave}, \tag{14}$$

$$S_{ave} = \frac{1}{6}(S_{i-1,j,k} + S_{i+1,j,k} + S_{i,j-1,k} + S_{i,j+1,k} + S_{i,j,k-1} + S_{i,j,k+1}), \tag{15}$$

where $S_{i,j,k}$ and $\widehat{S}_{i,j,k}$ are the source term before and after the smoothing scheme is applied at the grid point (i,j,k), respectively. As stated in [44], the smoothing procedure is a conservative scheme, in contrast to the high-wavenumber energy truncation associated with pseudo-spectral simulations or filtering in large-eddy simulation, both of which result in losses of the coupling terms appearing in the gas phase transport equations. If the smoothing scheme is not applied, the droplet source terms are distributed onto the nearest eight grid points. If it is applied once, then the droplet contribution affects grid points further away from the nearest eight grid points. On the analogy of this, if it is applied twice, the droplet effects spread to more grid points which are further away than those affected if the smoothing scheme is applied once.

Since correlations between droplet source terms and gas phase flow variables will be examined, it is vital to first affirm that the statistics is not dependent on the numerical procedure of how the droplet source terms are distributed onto Eulerian grids. For this purpose, we introduce a numerical parameter n_s, which indicates how many times the smoothing scheme is applied to the droplet source terms S_{ms}, $\vec{S}_{mo}$, and S_{en} in every time step of DNS, in addition to the physical parameter τ_v in the parametric study. For the droplet case with small evaporation delay $\tau_{v,0}$, it was found that the smoothing scheme must be applied to attenuate the spatial "spottiness" of the source terms, which leads to artificial oscillations in the simulation results as low-dissipation compact finite-difference schemes are employed [44], and thus to stabilise the DNS. Therefore n_s is set to 1 and 2, with the former case designated as Dh_sn1 and the latter Dh_sn2, as shown in Table 1. For big evaporation delay $\tau_v = \tau_{v,\infty}$, n_s is 0 for Case Dh_bn0 and 1 for Case Dh_bn1.

In Table 1, special case labels are used to facilitate distinguishing different cases. "RML" designates the droplet-free Reacting Mixing Layer. The names of all the droplet cases start with the letter "D". The subscript to the second letter "h" illustrates the magnitude of the latent heat of vapourisation, "s" and "b" for "$h_{fg} = h_0$ (small)", "$h_{fg} = h_\infty$ (big)", respectively. The number following the next letter "n" indicates the value of n_s, i.e., the times of the application of the smoothing scheme to the droplet source terms S_{ms}, $\vec{S}_{mo}$, and S_{en} in every time step of DNS.

The grid numbers used are $n_x \times n_y \times n_z = 384 \times 768 \times 232 = 68{,}419{,}584$. The grid spacing is uniform in each direction, $\Delta x = \Delta y \approx \Delta z \approx 0.076$, and on the order of the Kolmogorov scale η of the fully developed turbulent mixing layer at $t = t_0$. η is estimated by $\eta = [(\tilde{\nu}/Re)^3/(|\epsilon_k|/\bar{\rho}_g)]^{1/4}$, where the kinematic viscosity $\tilde{\nu}$ is $\tilde{\nu} = \bar{\mu}/\bar{\rho}_g$. The ratio of the minimal Kolmogorov scale across the mixing layer to the grid spacing is $\eta_{min}/\max(\Delta x, \Delta z) = 0.55$ at $t = t_0$. The initial droplet diameter which corresponds to $St_0 = 1$ is $D_{d,0} \approx 4.66 \times 10^{-3}$. This is approximately 6.18% of the grid spacing, therefore the point-source approach is justified. The volume fraction of all the droplets initially embedded in the carrier phase is $MLR_0/(\rho_d/\rho_{g,0}) \approx 0.48 \times 10^{-3}$. It is well below the threshold value 1×10^{-3}, above which the turbulence of the carrier phase can be affected by droplet–droplet collisions [39]. Consequently, the two-phase flow is a dilute fluid-droplet mixture and droplet–droplet interactions can be neglected.

For both the gas and droplet phases, periodic boundary conditions are applied in the streamwise x and spanwise z directions, while non-reflecting boundary conditions [46] are imposed in the cross-stream direction y for the gas phase. Droplets are assumed not to enter the computational domain again if they move out of the cross-stream boundaries at $y = -L_y/2$ and $y = L_y/2$. At $t = t_0$, 98.8% of the initially embedded droplets are retained in the computational domain. The droplet loss at the cross-stream boundaries is thus negligible.

The spatial derivatives are calculated by a 6th-order compact finite difference scheme [47]. Time advancement for the gas and droplet phase is achieved by a 3rd-order explicit Runge–Kutta method and a first-order quasi-steady-state approach [48], respectively.

To trace close to 17×10^6 droplets, the simulations were performed on the UK national high-end supercomputer HECToR using 384 MPI processes.

3. Results and discussion

The effective Reynolds number Re_ω, defined as $Re_\omega = Re\delta_\omega/\delta_{\omega,0}$, is $Re_\omega = 10{,}121$ for the turbulent mixing layer at $t = t_0$. Figure 2a exemplifies the turbulent flow using the spanwise and streamwise vorticity at two boundary planes $z = 0$ and $x = 0$ at $t = t_0$. The droplet distributions at the two planes are shown in Fig. 2b. The selective droplet locations in the turbulent flow can be seen. The stoichiometric mixture fraction Z_{st} is also shown by bold red lines, indicating where combustion will take place and where combustion-released heat will be initiated.

Intense interactions between turbulent combustion and evaporating droplets occur immediately after $t = t_0$. For the droplet-free reacting mixing layer case RML, the integrated mean reaction rate across the mixing layer $\int_{x_2} \bar{\omega}_T dx_2$ is found substantial shortly after the reaction is enabled (not shown), since the fuel and the oxidiser are allowed to mix up to $t = t_0$ before combustion occurs. At $t = t_0 + 0.1\tau_t$, the reaction is predominantly controlled by mixing and thus becomes much weaker. For the droplet cases Dh_sn1 and Dh_sn2, droplets evaporate abruptly due to the small characteristic evaporation time scale $\tau_{v,0}$. At $t = t_0 + 0.1\tau_t$, the number of residual droplets in the central region of the turbulent mixing layer considerably decreases. A stage will be soon attained, in which the turbulent mixing layer is predominantly affected by vapour diffusion rather than droplet evaporation [43]. For Cases Dh_bn0 and Dh_bn1, considerable heat exchange takes place between the two phases to drive droplet evaporation. At $t = t_0 + 0.1\tau_t$, the gas temperature T_g has been decreased considerably and is approaching the ambient gas temperature $T_{g,0}$. In view of the intense interactions among turbulence, combustion, and inert droplets during $[t_0, t_0 + 0.1\tau_t]$, the droplet and combustion effects on turbulence in this time period is first scrutinised in Section 3.1.

To achieve systematic understanding of the turbulence–combustion–droplets interactions in the turbulent multi-phase reacting flow, the statistics in the period $t \in [t_0 + 0.9\tau_t, t_0 + \tau_t]$ is also obtained to investigate the droplet and combustion effects on turbulence as the temporally-developing two-phase reacting mixing layers approach their respective self-similar states. The analysis is detailed in Section 3.2.

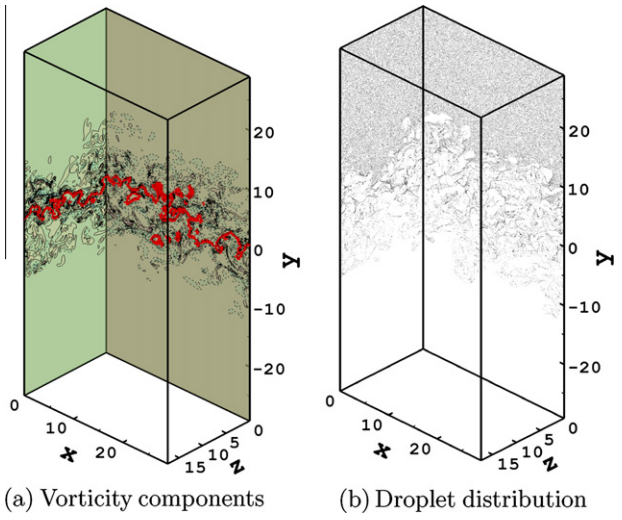

Fig. 2. The instantaneous turbulent flow field and droplet distribution at $t = t_0 = 225$. In (a), the spanwise vorticity ω_z at the boundary plane $z = 0$ and the streamwise vorticity ω_x at the boundary plane $x = 0$ are shown. Twenty contour levels evenly distributed within the range of $[-2.26, 2.31]$ and $[-1.94, 2.61]$ are used for ω_z and ω_x, respectively, with solid lines indicating positive values and dashed lines negative ones. The bold red lines designate the locations of the stoichiometric mixture fraction Z_{st} in the two planes. In (b), droplets located within half grid spacing away from the according two planes are shown. The number of droplets shown at the plane $z = 0$ and $x = 0$ is 72,347 and 45,651, respectively. (For interpretation of the references to colour in this figure legend, the reader is referred to the web version of this article.)

3.1. $t \in [t_0, t_0 + 0.1\tau_t]$

To investigate the combustion and droplet effects on turbulence, it is instructive to first examine the turbulence kinetic energy of the mixing layer for all the cases. For this purpose, temporal evolution of the TKE integrated across the mixing layer $\int_{x_2} \bar{\rho}_g k dx_2$ during $t \in [t_0, t_0 + 0.1\tau_t]$ is presented in Fig. 3. The ordinate is normalised by K_0 the integrated TKE at $t = t_0$, i.e., $K_0 = \int_{x_2} \bar{\rho}_g k dx_2\big|_{t=t_0} = \int_y \bar{\rho}_g k dy\big|_{t=t_0}$. Both x_2 and y indicate the cross-stream direction. It is clear that the TKEs increase for all the cases, in part due to the "combustion-generated turbulence" [11,20]. For Cases Dh_bn0 and Dh_bn1, combustion-released heat is considerably taken away by the inert droplets to drive evaporation, as the comparison of the gas temperature field shown in Fig. 4c with that in Fig. 4a would imply. Consequently, the TKE is found lower than that for Case RML. On the other hand, the TKEs for Cases Dh_sn1 and Dh_sn2 become bigger than that for Case RML, which is due to other mechanisms and needs further investigation.

To detail the analysis of the effects of combustion, droplet dynamics and evaporation on flow turbulence, the TKE transport equation for the multi-phase reacting flow is used, which can be written as

$$\frac{\partial}{\partial t}(\bar{\rho}_g k) + \frac{\partial}{\partial x_i}(\bar{\rho}_g k \tilde{u}_{g,i}) = -\overline{\rho_g u''_{g,i} u''_{g,j}} \frac{\partial \tilde{u}_{g,i}}{\partial x_j} - \frac{\partial}{\partial x_j}\left(\frac{1}{2}\overline{\rho_g u''_{g,i} u''_{g,i} u''_{g,j}}\right) - \frac{\partial}{\partial x_i}\overline{p u''_{g,i}} + \overline{p \frac{\partial u''_{g,i}}{\partial x_i}} + \frac{\partial}{\partial x_i}\overline{u''_{g,j}\sigma_{ij}} - \overline{\frac{\partial u''_{g,j}}{\partial x_i}\sigma_{ij}} + \overline{\mathbb{F}_{drag,i} u''_{g,i}} + \overline{\mathbb{E}_{drag,i} u''_{g,i}} + \frac{1}{2}\overline{\dot{\mathbb{M}}_d u''_{g,i} u''_{g,i}}. \quad (16)$$

In the three droplet-related terms, $\mathbb{F}_{drag,i}$, $\mathbb{E}_{drag,i}$ and $\dot{\mathbb{M}}_d$ are defined as

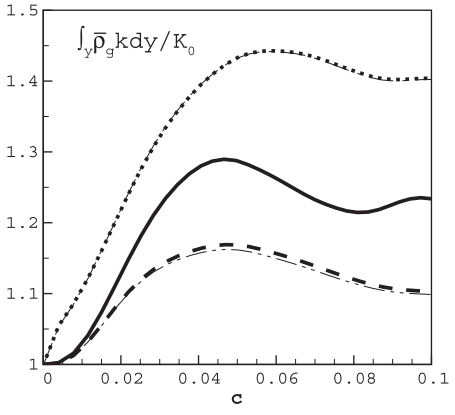

Fig. 3. Temporal evolution of the integrated turbulence kinetic energy in the time period $[t_0, t_0 + 0.1\tau_t]$. The abscissa denotes the time, i.e., $0 \leqslant c \leqslant 0.1 \Leftrightarrow t_0 \leqslant t \leqslant t_0 + 0.1\tau_t$. The ordinate is normalised by K_0 the integrated TKE at $t = t_0$, i.e., $K_0 = \int_{x_2} \bar{\rho}_g k dx_2\big|_{t=t_0}$. The solid, dotted, dash-dot, dashed, and dash-dot-dot lines denote Case RML, Dh_sn1, Dh_sn2, Dh_bn0, and Dh_bn1, respectively. The line captions apply to all the line plots in the paper, unless otherwise specified.

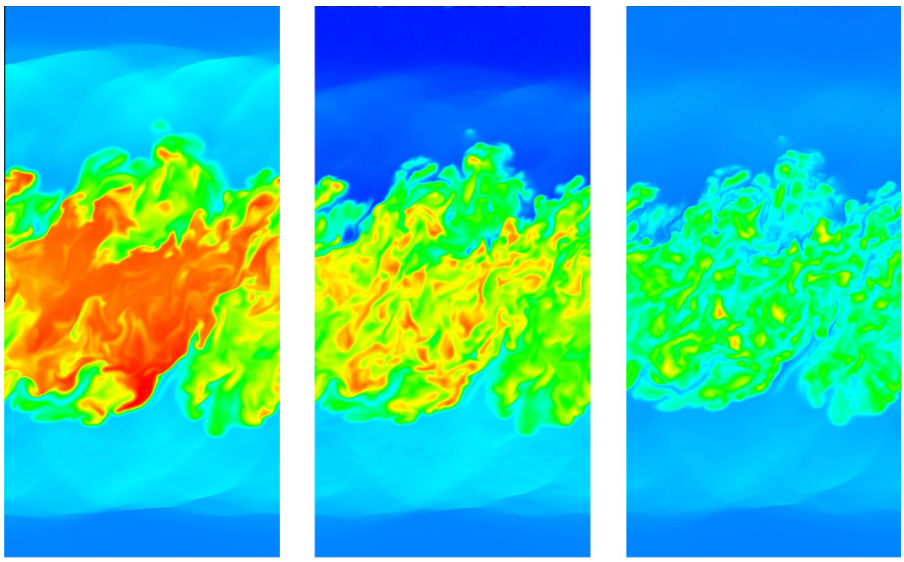

Fig. 4. The temperature contour plots at the central plane in the spanwise direction $z = L_z/2$ at $t = t_0 + 0.1\tau_t$. The same contour range [0.78, 2.47] is employed for all the three cases. Case RML is the reacting mixing layer without droplets. For Case Dhsn1, the latent heat of vaporisation h_{fg} is small and therefore droplet evaporation is intense. For Case Dhbn0, h_{fg} is big, leading to considerable heat exchange between the two phases.

$$\mathbb{F}_{\mathrm{drag},i} = -\frac{1}{V}\sum_k F_{\mathrm{drag},k,i} = -\frac{1}{V}\sum_k \left[f_k \frac{m_{\mathrm{d},k}}{St_k}(u_{\mathrm{g},k,i} - v_{\mathrm{d},k,i})\right] = -\frac{1}{V}\sum_k \left[3\pi\frac{\mu}{Re}\cdot f_k \cdot D_{\mathrm{d},k}(u_{\mathrm{g},k,i} - v_{\mathrm{d},k,i})\right], \tag{17}$$

$$\mathbb{E}_{\mathrm{drag},i} = -\frac{1}{V}\sum_k [-\dot{m}_{\mathrm{d},k}(u_{\mathrm{g},i} - v_{\mathrm{d},k,i})] = -\frac{1}{V}\sum_k \left[\pi\frac{\mu}{ReSc}\cdot Sh_k H_{\mathrm{M},k}\cdot D_{\mathrm{d},k}(u_{\mathrm{g},i} - v_{\mathrm{d},k,i})\right], \tag{18}$$

$$\dot{\mathbb{M}}_{\mathrm{d}} = S_{\mathrm{ms}} = -\frac{1}{V}\sum_k \dot{m}_{\mathrm{d},k}. \tag{19}$$

Similarity can be discovered between Eqs. (17) and (18). Since $\mathbb{F}_{\mathrm{drag},i}$ is the aerodynamic drag force, $\mathbb{E}_{\mathrm{drag},i}$ is therefore designated as the "evaporating drag". As shown by Eq. (16), the direct droplet effects on turbulence can be categorised in three parts, i.e., the power due to the aerodynamic drag between the phases, the power due to the evaporating drag, and an additional production rate due to evaporation. It is easy to demonstrate that the last term $0.5\overline{\dot{\mathbb{M}}_{\mathrm{d}}u''_{\mathrm{g},i}u''_{\mathrm{g},i}}$ is always positive for evaporation and thus produce TKE. It should be pointed out that in the present study with combustion-released heat, condensation of inert evaporated vapour can be neglected.

In Eq. (16), all the gradient terms, including the mean convection $\partial(\bar{\rho}_{\mathrm{g}}k\tilde{u}_{\mathrm{g},i})/\partial x_i$, triple correlation $-\partial\left(0.5\overline{\rho_{\mathrm{g}}u''_{\mathrm{g},i}u''_{\mathrm{g},i}u''_{\mathrm{g},j}}\right)\big/\partial x_j$, pressure–velocity correlation $-\partial\overline{pu''_{\mathrm{g},i}}/\partial x_i$, and the viscous diffusion $\partial\overline{u''_{\mathrm{g},j}\sigma_{ij}}/\partial x_i$, will not be considered in the analysis, since they redistribute TKE via various mechanisms, but do not produce or dissipate TKE as the other terms do. To exclude the redistributive terms from the analysis, Eq. (16) is integrated across the mixing layer. The turbulence production rate $-\overline{\rho_{\mathrm{g}}u''_{\mathrm{g},i}u''_{\mathrm{g},j}}\partial\tilde{u}_{\mathrm{g},i}/\partial x_j$ and dissipation rate $-\overline{\left(\partial u''_{\mathrm{g},j}/\partial x_i\right)\sigma_{ij}}$, the pressure-dilation $\overline{p\partial u''_{\mathrm{g},i}/\partial x_i}$, and the three droplet-related terms will be examined in their integrated forms to analyse how the turbulence is affected by combustion and inert evaporating droplets. The integrated TKE transport equation for the multi-phase reacting flow can be written as:

$$\frac{d}{dt}\int_{x_2} K\,dx_2 = \int_{x_2} P_k\,dx_2 + \int_{x_2}\Phi_k\,dx_2 + \int_{x_2}\epsilon_k\,dx_2 + \int_{x_2} F_k\,dx_2 + \int_{x_2} E_k\,dx_2 + \int_{x_2} M_k\,dx_2, \tag{20}$$

where the turbulence kinetic energy K, production rate P_k, pressure-dilatation Φ_k, dissipation rate ϵ_k, and the droplet source terms: power due to aerodynamic drag F_k, power due to "evaporating drag" E_k, and production rate due to evaporation M_k, are defined as

$$K \equiv \frac{1}{2}\overline{\rho_{\mathrm{g}}u''_{\mathrm{g},i}u''_{\mathrm{g},i}}, \tag{21}$$

$$P_k \equiv -\overline{\rho_{\mathrm{g}}u''_{\mathrm{g},i}u''_{\mathrm{g},j}}\frac{\partial\tilde{u}_{\mathrm{g},i}}{\partial x_j}, \tag{22}$$

$$\Phi_k \equiv \overline{p\frac{\partial u''_{\mathrm{g},i}}{\partial x_i}}, \tag{23}$$

$$\epsilon_k \equiv -\overline{\frac{\partial u''_{\mathrm{g},j}}{\partial x_i}\sigma_{ij}}, \tag{24}$$

$$F_k \equiv \overline{\mathbb{F}_{\mathrm{drag},i}u''_{\mathrm{g},i}}, \tag{25}$$

$$E_k \equiv \overline{\mathbb{E}_{\mathrm{drag},i}u''_{\mathrm{g},i}}, \tag{26}$$

$$M_k \equiv \frac{1}{2}\overline{\dot{\mathbb{M}}_{\mathrm{d}}u''_{\mathrm{g},i}u''_{\mathrm{g},i}}. \tag{27}$$

The definition of ϵ_k is rewritten in Eq. (24) to have a complete list of the definitions of the budget terms in Eq. (20).

Figure 5 presents temporal evolution of the budget terms in the integrated TKE transport Eq. (20) in the period $[t_0, t_0 + 0.1\tau_t]$. To facilitate comparison, the ordinates are normalised by E_0 the magnitude of the integrated turbulence dissipation rate at $t = t_0$, $E_0 = \left|\int_{x_2}\epsilon_k\,dx_2\right|_{t=t_0}$. It can be seen that the pressure-dilatation effect plays a dominant role for the variation of the TKE. $\int_{x_2}\Phi_k\,dx_2$ is close to one order of magnitude bigger than the integrated production $\int_{x_2}P_k\,dx_2$ and dissipation rate $\int_{x_2}\epsilon_k\,dx_2$. This is consistent with the results of DNS of a droplet-free reacting mixing layer [20]. The pressure-dilatation contributes mainly

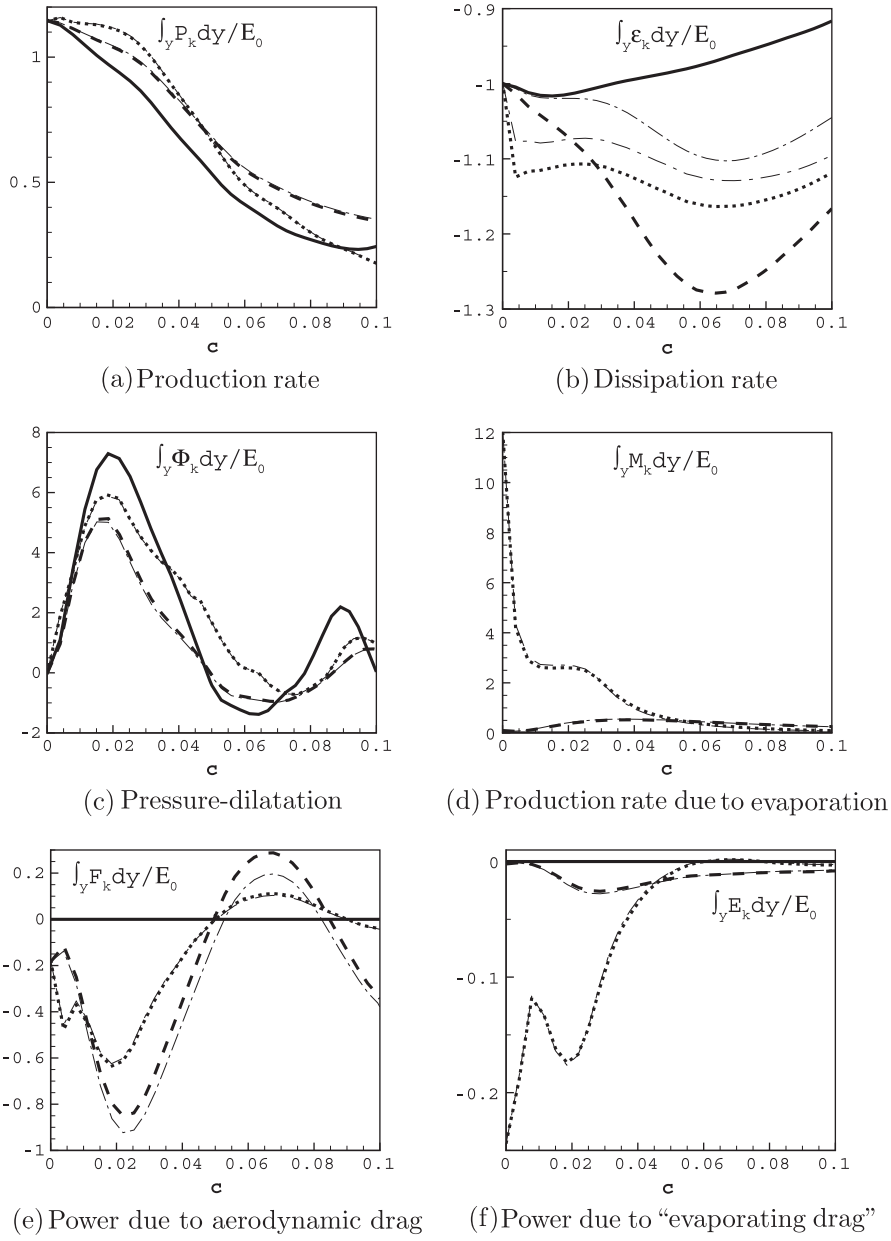

Fig. 5. Temporal evolution of integrated terms in the TKE transport Eq. (20) in the time period $[t_0, t_0 + 0.1\tau_t]$. The ordinates are normalised by E_0 the magnitude of the integrated turbulence dissipation rate at $t = t_0$, i.e., $E_0 = \left|\int_{x_2} \epsilon_k \, dx_2\right|_{t=t_0}$.

positively to the TKE, although fluctuating around 0. Since the pressure-dilatation term exchanges energy between internal energy and turbulence kinetic energy [22], the energy is overall transferred from internal energy to TKE at strong exothermicity for all the cases. For the evaporation-intense cases Dh_sn1 and Dh_sn2, the magnitude of the term is smaller than for Case RML, followed by those for Cases Dh_bn0 and Dh_bn1. Pressure-dilatation is known to be determined by the combustion-released heat, which is extracted by the inert droplets to drive evaporation in the present study. Shown in Fig. 4 are the contour plots of the gas temperature T_g at the plane $z = L_z/2$ at $t = t_0 + 0.1\tau_t$ for Cases RML, Dh_sn1, and Dh_bn0. The results of the other two cases Dh_sn2 and Dh_bn1 are not shown due to their resemblance to that of Dh_sn1 and Dh_bn0, respectively. It can be seen that T_g has been significantly decreased by the droplets and heat release diminished for Case Dh_bn0; While for Case Dh_sn1, the gas temperature is moderated by still high, leading to stronger pressure-dilatation effect than for Case Dh_bn0.

The pressure-dilatation correlation can be further decomposed into mechanical work due to mean pressure and pressure fluctuation, i.e., $\overline{p\partial u''_{g,i}/\partial x_i} = \bar{p}\partial\overline{u''_{g,i}}/\partial x_i + \overline{p'\partial u''_{g,i}/\partial x_i}$. The second term on the right-hand side was found to be the predominant term for the pressure-dilatation, showing very similar profile to the pressure-dilatation and being one order of magnitude bigger than the first term for all the cases (not shown). Therefore, the pressure-dilatation is determined by the correlation between the pressure fluctuation and dilatation, i.e., $\overline{p\partial u''_{g,i}/\partial x_i} \approx \overline{p'\partial u''_{g,i}/\partial x_i}$. The droplet effects on the two terms show similar trends as in Fig. 5c, that is, diminishing as the gas temperature decreases.

The dilatation or volume expansion can be reflected in the Favre-mean cross-stream velocity, as exemplified in Fig. 6 at

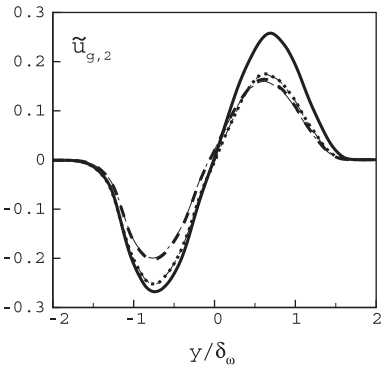

Fig. 6. The Favre-mean cross-stream gas velocity at $t = t_0 + 0.05\tau_t$.

$t = t_0 + 0.05\tau_t$. The positive cross-stream velocity in the upper stream and negative velocity in the lower stream indicate the volume is expanding due to the combustion-released heat. The magnitude of $\tilde{u}_{g,2}$ for Case RML is the biggest, followed by those for Cases Dh_sn1, Dh_sn2 and for Cases Dh_bn0, Dh_bn1 due to diminished thermal expansion.

For all the droplet-related terms shown in Fig. 5d–f, excellent agreement between Case Dh_sn1 and Dh_sn2, and between Case Dh_bn0 and Dh_bn1, on the statistics of correlations between droplet source terms ($\overrightarrow{\mathbb{F}}_{drag}$, $\overrightarrow{\mathbb{E}}_{drag}$, and $\dot{\mathbb{M}}_d$) and gas velocity fluctuations has been achieved. This demonstrates that different droplet-source-term distribution methods have negligible influence on these flow-droplet correlation terms. The key difference between the droplet cases is that for Cases Dh_sn1 and Dh_sn2, the magnitude of the additional integrated production rate due to evaporation $\int_{x_2} M_k\,dx_2$ is significantly bigger than that for Cases Dh_bn0 and Dh_bn1. The source term exceeds the magnitude of the integrated pressure-dilation $\int_{x_2} \Phi_k\,dx_2$ immediately after the reaction and droplet effects are enabled at $t = t_0$. Clearly, it is $\int_{x_2} M_k\,dx_2$ which largely contributes to the increase of the TKE for Cases Dh_sn1 and Dh_sn2 in addition to pressure-dilatation. In contrast, $\int_{x_2} M_k\,dx_2$ for Cases Dh_bn0 and Dh_bn1 slowly increases towards a small positive value, whose magnitude is negligible compared to that for Cases Dh_sn1 and Dh_sn2. As a consequence, the TKE increases but reaches a lower value than for Case RML with reduced pressure-dilation effect and negligible additional production rate due to evaporation. In summary, with the TKE increasing for all the cases, the contribution of the additional production rate due to evaporation $\int_{x_2} M_k\,dx_2$ makes the TKE the biggest for Cases Dh_sn1 and Dh_sn2.

For the other two droplet terms $\int_{x_2} F_k dx_2$ and $\int_{x_2} E_k\,dx_2$, the correlation $\overline{(u_{g,i} - v_{d,i})u''_{g,i}}$ appears in both F_k and E_k. In previous DNS studies of solid-particle-laden incompressible, isothermal flow, such as homogeneous isotropic [49] and shear [50] turbulence, the comparisons between the autocorrelation of the turbulent velocity of the gas phase or the normal turbulent stresses $\overline{u''_{g,i}u''_{g,i}}$ and the correlation between the turbulent velocity of the gas phase and that of the droplets $\overline{u''_{g,i}v''_{d,i}}$ were scrutinised to reveal the physical mechanism of particle effects on turbulence. For the current compressible turbulence with mean shear, strong heat release and laden with evaporating droplets, inspection of the two correlations leads to the conclusion that the difference between the two cannot be the sole factor determining the contribution of the two gas-droplet correlation terms $\int_{x_2} F_k\,dx_2$ and $\int_{x_2} E_k\,dx_2$ to flow turbulence. The nonlinearity stemming from the correlation among the evaporation which changes the droplet diameter D_d, droplet dynamics which is strongly affected by evaporation [42], and flow turbulence, must be fully taken into account before the modelling of the mechanical work done by the aerodynamic and evaporating drags can be attempted, which poses grand challenges for modelling the droplet effects on turbulent reacting flow.

Overall, the direct droplet effect due to $\int_{x_2} F_k\,dx_2$ is close to one order of magnitude bigger than the effect due to $\int_{x_2} E_k\,dx_2$, comparing Fig. 5e with f. $\int_{x_2} F_k\,dx_2$ is on the same magnitude as that of the integrated production and dissipation rates, which are shown in Fig. 5a and b, respectively. The magnitude of the integrated power due to aerodynamic drag $\int_{x_2} F_k\,dx_2$ is bigger for Cases Dh_bn0 and Dh_bn1, while the magnitude of the integrated power due to evaporating drag $\int_{x_2} E_k\,dx_2$ is bigger for Cases Dh_sn1 and Dh_sn2 initially, but decreases rapidly towards 0. It is also interesting to note that the profile of $\int_{x_2} \Phi_k\,dx_2$ shown in Fig. 5c is similar to that of $\int_{x_2} F_k\,dx_2$ shown in Fig. 5e except for opposite signs for the two terms. This may imply that the pressure-dilatation effect imposes direct impact on the mechanical work done by the interphase drag at strong exothermicity.

The turbulence production rate P_k describes the transfer of kinetic energy from mean flow to fluctuating motion. For a temporal mixing layer, the product of the turbulent shear stress $-\overline{\rho_g u''_{g,1}u''_{g,2}}$ and the mean shear $\partial\tilde{u}_{g,1}/\partial x_2$ determines the profile of turbulence production rate. Figure 5a shows that the integrated turbulence production rate $\int_{x_2} P_k\,dx_2$ decreases for all the cases. The reduction of turbulence production rate in an exothermic mixing layer was also found in [19]. The droplets slow the decrease of $\int_{x_2} P_k\,dx_2$ due to the thermal energy exchange between the two phases. Since the difference of $\int_{x_2} P_k\,dx_2$ between the droplet-free and droplet-laden cases is small, it can be said that the combustion effect is predominant over the droplet effect on turbulent production rate due to the strong combustion-released heat during $[t_0, t_0 + 0.1\tau_t]$.

Compared to the slight increase of the integrated turbulence production rate $\int_{x_2} P_k\,dx_2$ due to the droplets as shown in Fig. 5a, the magnitude of the integrated turbulence dissipation rate $\int_{x_2} \epsilon_k\,dx_2$ is considerably increased by the droplets, as shown in Fig. 5b. It is worth mentioning that in previous papers [37,41,42], the dissipation rate χ of the mixture fraction variance Z''^2 was also found to be enhanced by the droplets.

The turbulence dissipation rate ϵ_k can be written as

$$\epsilon_k \approx -\overline{\frac{\partial u''_{g,j}}{\partial x_i}\sigma''_{ij}} = -\overline{s''_{ij}\sigma''_{ij}} = -2\frac{\mu}{Re}\left(\overline{s''_{ij}s''_{ij}} - \frac{\overline{s''_{ii}s''_{jj}}}{3}\right), \tag{28}$$

where s''_{ij} is the fluctuating component of the strain rate, i.e., $s''_{ij} = 0.5\left(\partial u''_{g,i}/\partial x_j + \partial u''_{g,j}/\partial x_i\right)$; σ''_{ij} is the fluctuating component of the stress tensor, $\sigma''_{ij} = 2\mu/Re\left(s''_{ij} - \delta_{ij}s''_{kk}/3\right)$. The Favre-mean component of σ_{ij} has been neglected due to the secondary contribution of $-\overline{\partial u''_{g,j}/\partial x_i\tilde{\sigma}_{ij}}$ to ϵ_k, where $\tilde{\sigma}_{ij} = 2\mu/Re(\widetilde{S}_{ij} - \delta_{ij}\widetilde{S}_{kk}/3)$. The Favre-mean strain rate $\widetilde{S}_{ij}$ is $\widetilde{S}_{ij} = 0.5(\partial\tilde{u}_{g,i}/\partial x_j + \partial\tilde{u}_{g,j}/\partial x_i)$. Since the dynamic viscosity μ is a constant in the present study, the TDR is fully determined by the two terms on the right-hand side of Eq. (28), denoting the squared strain rate magnitude and the squared dilatation magnitude. The squared dilatation magnitude is equivalent to the dilatation dissipation [51], which was defined to account for the compressibility effect on TDR.

The temporal evolution of the integrated squared strain rate magnitude $\int_{x_2} \overline{s''_{ij}s''_{ij}}\,dx_2$ and squared dilatation magnitude $\int_{x_2} \overline{s''_{ii}s''_{jj}}\,dx_2$ is shown in Fig. 7a and b, respectively. Before analysis is furthered, it should be first pointed out that as shown in Figs. 5b and 7a, the statistical difference between Case Dh_bn0 and Dh_bn1 demonstrates that the times of the application of the smoothing scheme to the droplet source terms S_{ms}, $\overrightarrow{S}_{mo}$, and S_{en} in every time step of DNS, denoted as n_s, affects most the integrated turbulence dissipation rate $\int_{x_2} \epsilon_k\,dx_2$ and squared strain rate magnitude $\int_{x_2} \overline{s''_{ij}s''_{ij}}\,dx_2$.

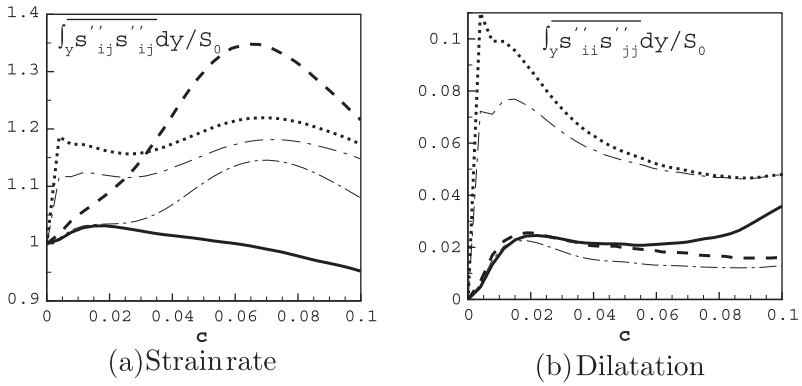

Fig. 7. Temporal evolution of the integrated squared strain rate magnitude and squared dilatation magnitude in the time period $[t_0, t_0 + 0.1\tau_t]$. The ordinates are normalised by S_0 the integrated squared strain rate magnitude at $t = t_0$, i.e., $S_0 = \int_{x_2} \overline{s''_{ij}s''_{ij}}\, dx_2\big|_{t=t_0}$.

As will be shown below, since the $St_0 \sim 1$ droplets locate in low vorticity, high strain-rate regions in turbulent flow, the momentum exchange via $\overline{F}_{\text{drag}}$ and the mass addition to the gas phase via evaporation impose direct impact on strain rate and in turn on dissipation rate. It can also be seen that the differences of $\int_{x_2} \overline{s''_{ij}s''_{ij}}\, dx_2$ and $\int_{x_2} \epsilon_k\, dx_2$ between Case Dh_bn0 and Dh_bn1 are bigger than those between Case Dh_sn1 and Dh_sn2, implying that the smoothing scheme affects more the coupling between the Eulerian gas phase and the Lagrangian droplets, if the droplet effects via the interphase aerodynamic drag on flow strain and dissipation dictate the coupling as for Cases Dh_bn0 and Dh_bn1.

As shown in Fig. 3, excellent agreement on the statistics of the integrated TKE has been achieved between Case Dh_sn1 and Dh_sn2 as well as between Case Dh_bn0 and Dh_bn1. This demonstrates that first, the turbulence dissipation rate ϵ_k is not a leading term which determines the variation of the TKE, as compared to the pressure-dilatation and the additional production rate due to evaporation shown in Fig. 5c and d, respectively. Second, the statistical differences of the integrated squared strain rate magnitude $\int_{x_2} \overline{s''_{ij}s''_{ij}}\, dx_2$ and dissipation rate $\int_{x_2} \epsilon_k\, dx_2$ between the droplet cases, both of which are below 20%, are acceptable for the study of turbulence–combustion–droplets interactions in the present study.

After concluding the effect of the parameter n_s on the statistics, we are now continuing the analysis of the effects of combustion and droplets on turbulence dissipation rate ϵ_k, which is determined by the squared strain rate magnitude $\overline{s''_{ij}s''_{ij}}$ and the squared dilatation magnitude $\overline{s''_{ii}s''_{jj}}$.

In incompressible flow, dilatation is absent. In the current compressible reacting flow, Fig. 7 shows that the integrated squared dilatation magnitude $\int_{x_2} \overline{s''_{ii}s''_{jj}}\, dx_2$ is at least one order of magnitude smaller than the integrated squared strain rate magnitude $\int_{x_2} \overline{s''_{ij}s''_{ij}}\, dx_2$, which is augmented by the droplets. Since dilatation is a quantitative measure of the volume change of fluid elements, the integrated squared dilatation magnitude $\int_{x_2} \overline{s''_{ii}s''_{jj}}\, dx_2$ rapidly increases due to thermal expansion for Case RML after reaction is enabled, as shown in Fig. 7b. The difference between Case RML and Case Dh_bn0 before $t \approx t_0 + 0.05\tau_t$ is hardly discernible. Thereafter, $\int_{x_2} \overline{s''_{ii}s''_{jj}}\, dx_2$ becomes smaller for Case Dh_bn0, since the gas temperature has been considerably decreased and the thermal expansion effect is not as strong as for Case RML. The difference between Case RML and Dh_bn1 becomes evident after $t = t_0 + 0.02\tau_t$ due to the application of the smoothing scheme. The difference of the statistics $\int_{x_2} \overline{s''_{ii}s''_{jj}}\, dx_2$ between Case Dh_bn0 and Dh_bn1 is small. It is interesting to note that for Case Dh_sn1, $\int_{x_2} \overline{s''_{ii}s''_{jj}}\, dx_2$ increases sharply to far bigger a value than those for Cases RML, Dh_bn0, and Dh_bn1. Comparing Case Dh_sn1 with Dh_sn2, although a second application of the smoothing scheme leads to smaller peak of $\int_{x_2} \overline{s''_{ii}s''_{jj}}\, dx_2$, the rapid rise of the integrated squared dilatation magnitude to a considerably bigger peak than those for Cases RML, Dh_bn0, and Dh_bn1, is also evident. From the continuity equation, it can be easily shown that $\partial u_{g,i}/\partial x_i = -(1/\rho_g)D\rho_g/Dt + (1/\rho_g)S_{\text{ms}}$, where D/Dt is the material derivative. For Cases Dh_bn0 and Dh_bn1, droplet evaporation is weak and thus the mass source term S_{ms} is small, the dilatation is determined by the gas density, which is largely affected by thermal expansion after reaction is enabled. For Cases Dh_sn1 and Dh_sn2, droplet evaporation is intense and contribute predominantly to the dilatation.

For Cases Dh_sn1 and Dh_sn2, the integrated squared strain rate magnitude $\int_{x_2} \overline{s''_{ij}s''_{ij}}\, dx_2$ reaches their first peak shortly after $t = t_0$; While for Cases Dh_bn0 and Dh_bn1, $\int_{x_2} \overline{s''_{ij}s''_{ij}}\, dx_2$ gradually increases towards their respective peak. Although the peak magnitudes of $\int_{x_2} \overline{s''_{ij}s''_{ij}}\, dx_2$ in Fig. 7a and of $\int_{x_2} \epsilon_k\, dx_2$ in Fig. 5b differ by close to 20% for Cases Dh_bn0 and Dh_bn1, the peaks appear at similar time instants, i.e., $t = t_0 + 0.07\tau_t$. Overall, the droplet effects on the integrated squared strain rate magnitude show very similar trend to the droplet effects on the integrated TDR magnitude as shown in Fig. 5b.

Compared to the combustion effect on the TDR shown in Fig. 5b for Case RML, the droplet effects on the TDR is much more evident, i.e., the TDR magnitude has been largely increased by the droplets. Since TDR is dominated by the squared strain rate magnitude, physical phenomena that affect the strain rate directly will in turn have significant effects on TDR. For the turbulent non-premixed flame in the present study, combustion predominantly takes place in the vicinity of the iso-surfaces where the mixture fraction Z equals to the stoichiometric value $Z = Z_{\text{st}}$. The correlation between Z_{st} and the strain rate is low, i.e., the locations of Z_{st} do not match those of high strain rate, as Fig. 2a would imply. In contrast, the $St_0 = 1$ droplets tend to centrifuge from vortical cores and move towards and accumulate in the low vorticity, high strain rate regions in turbulent flow [24,25,42]. Therefore, as intense evaporation occurs for Cases Dh_sn1 and Dh_sn2 or momentum exchange with the carrier phase starts for Cases Dh_bn0 and Dh_bn1, evaporation and/or droplet dynamics exhibit much more direct impact on the strain rate, and in turn on the TDR, compared to combustion.

Although the initial droplet dynamic response time scale is identical for all the droplet cases, i.e., $St_0 = 1$, their characteristic evaporation time scales τ_v are very different. For Cases Dh_sn1 and Dh_sn2, τ_v is small, $\tau_v = \tau_{v,0}$, and thus the integrated squared strain rate magnitude $\int_{x_2} \overline{s''_{ij}s''_{ij}}\, dx_2$ rises sharply due to the evaporation effect. In contrast, $\int_{x_2} \overline{s''_{ij}s''_{ij}}\, dx_2$ increases gradually for Cases Dh_bn0 and Dh_bn1, since the evaporation time scale is large and the

droplets' effect on strain rate is dominated by the interphase drag according to the dynamic response time scale.

Another idealised case has been arranged to "isolate" the evaporation and dynamic effects of the droplets on turbulence, in which the interphase drag was disabled and only the evaporation effect was retained with the characteristic evaporation time set to $\tau_{v,0}$ and n_s set to 1. It is confirmed that the initial sharp rise of the integrated squared strain rate magnitude $\int_{x_2} \overline{s''_{ij}s''_{ij}}\,dx_2$ for Cases $\mathrm{Dh_sn1}$ and $\mathrm{Dh_sn2}$ is indeed due to evaporation, since whether or not the drag term exists shows negligible difference between the idealised case and Case $\mathrm{Dh_sn1}$ up to $t = t_0 + 0.03\tau_t$ (not shown). Due to rapid evaporation, considerable amount of droplets continuously disappear. The droplet number N_d is N_d = 16,718,959, 13,823,386 (=82.7% $N_{d,0}$), and 11,877,614 (=71.0% $N_{d,0}$) at $t = t_0$, $t_0 + 0.05\tau_t$, and $t_0 + 0.1\tau_t$, respectively, for Case $\mathrm{Dh_sn1}$. Consequently notable evaporation effect is observed shortly after the reaction and droplet effects are enabled at $t = t_0$. Thereafter, the integrated squared strain rate magnitude maintains at the enhanced level and does not increase further notably for Cases $\mathrm{Dh_sn1}$ and $\mathrm{Dh_sn2}$.

To further demonstrate the significance of droplet distribution on droplet evaporation, which imposes direct impact on flow strain and in turn on the TDR, we show in Fig. 8a a scatter plot of the vapour mass fraction Y_v normalised by its mean $\langle Y_v\rangle$, 0.15, against the cross-stream vorticity component ω_y normalised by its root-mean-square value $\omega_{y,\mathrm{rms}}$ at $t = t_0 + 0.01\tau_t$, shortly after the reaction and droplet effects are enabled at $t = t_0$, for Case $\mathrm{Dh_sn1}$. Both Case $\mathrm{Dh_sn1}$ and $\mathrm{Dh_sn2}$ reach their first peaks of $\int_{x_2} \overline{s''_{ij}s''_{ij}}\,dx_2$ close to $t = t_0 + 0.01\tau_t$, as shown in Fig. 7a. The data samples were collected from the plane $y = 0$ in the central region of the turbulent mixing layer. It can be seen that vapour is predominantly generated in the regions of low vorcitiy due to the preferential concentration of droplets in these regions. More systematically, Fig. 8b presents the normalised conditional expectation of Y_v against the normalised Π_d, the second invariant of the deformation tensor $\partial u_{g,i}/\partial x_j$. It is defined as $\Pi_d = -(S^2 - 1/4\omega_i\omega_i)/2$ [25], where S^2 is the square of the magnitude of the strain rate tensor and ω_i the ith component of vorticity. It conveniently quantifies high-vorticity-magnitude regions with $\Pi_d > 0$ and high-strain-rate-magnitude regions with $\Pi_d < 0$ in one plot. The conditional mean "$\langle\cdot|\cdot\rangle$" and the mean "$\langle\cdot\rangle$" in Fig. 8b were obtained in the central region of the turbulent mixing layer $-\delta_\omega/2 < y < \delta_\omega/2$. The span of the sample variable Π_d was divided into bins with identical width. It is clear that for Cases $\mathrm{Dh_sn1}$ and $\mathrm{Dh_sn2}$ at $t = t_0 + 0.01\tau_t$ the vapour is predominantly produced at low vorticity regions where droplets locate and evaporate, supporting the finding of Fig. 8a. In high strain rate regions as Π_d becomes negative and leaves the origin of the abscissa, the conditional mean $\langle Y_v|\Pi_d\rangle$ is smaller than the regional mean $\langle Y_v\rangle$, indicating that at this time the droplets align with low vorticity regions more than with high strain rate regions, and always avoid the vortical core regions where the vorticity magnitude is high and $\Pi_d > 0$.

The normalised conditional mean $\langle Y_v|\Pi_d\rangle/\langle Y_v\rangle$ at a later time $t = t_0 + 0.07\tau_t$, when the integrated squared strain rate magnitude $\int_{x_2} \overline{s''_{ij}s''_{ij}}\,dx_2$ and the integrated TDR magnitude reach their peak for Cases $\mathrm{Dh_bn0}$ and $\mathrm{Dh_bn1}$, is also presented for all the droplet cases. It shows that the conditional mean $\langle Y_v|\Pi_d\rangle$ in high vorticity regions where $\Pi_d > 0$ is close to the regional mean $\langle Y_v\rangle$. As evaporation continues, the droplet size decreases and droplets tend to move towards vortical cores [42]. Vapour is thus produced in these regions. Turbulent convection and diffusion can be the second mechanism to raise Y_v in these regions according to Eq. (5). Compared to the high vorticity regions, $\langle Y_v|\Pi_d\rangle$ increases almost monotonically as the strain rate magnitude increases, in contrast to the profiles at $t = t_0 + 0.01\tau_t$. This phenomenon can be explained as follows.

The interaction between the droplets and turbulence is bilateral. The low vorticity or high strain rate regions attract droplets of $St \sim 1$. On the other hand, the strain rate is dictated by the derivative of the gas velocity. It is expected that either evaporation or the interphase drag will generate velocity fluctuations, i.e., velocity gradient, in the turbulent flow, and thus increase the strain rate magnitude. As the droplets locate in the low vorticity or high strain rate regions, the effect of enhancing the strain rate magnitude is profound in comparison with the combustion effect, as shown in Fig. 7a. The mutual effects between the turbulent flow and evaporating droplets leads to the monotonic increase of $\langle Y_v|\Pi_d\rangle$ with the increase of the strain rate magnitude or $|\Pi_d|$.

Comparing Case $\mathrm{Dh_sn1}$ with $\mathrm{Dh_bn0}$, two major differences can be seen in the high strain rate regions where $\Pi_d < 0$ at $t = t_0 + 0.07\tau_t$ in Fig. 8b. First, the slope of the curve is steeper for Case $\mathrm{Dh_bn0}$, where evaporation is weak overall and the droplet size does not decrease significantly (see Fig. 9b). This implies that the tendency that evaporated vapour is found in high strain rate regions is more evident for Case $\mathrm{Dh_bn0}$ than for Case $\mathrm{Dh_sn1}$. Secondly, the conditional mean is about twice the regional mean for Case $\mathrm{Dh_bn0}$ in the highest strain rate regions compared to about $1.3 - 1.4$ times the regional mean for Case $\mathrm{Dh_sn1}$, further indicating that the vast majority of evaporation takes place in these regions.

Comparing Case $\mathrm{Dh_sn1}$ with $\mathrm{Dh_sn2}$, Case $\mathrm{Dh_bn0}$ with $\mathrm{Dh_bn1}$, it can be seen that the application of the smoothing scheme to the droplet source terms has more direct impact on the statistics in the

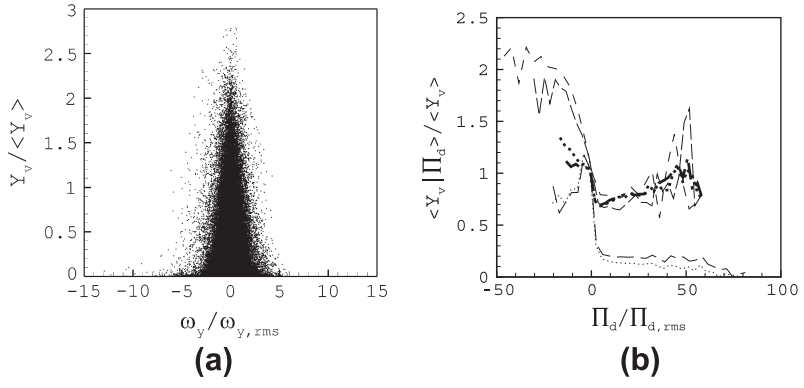

Fig. 8. (a) Scatter plot of the vapour mass fraction Y_v against the cross-stream vorticity component ω_y at $t = t_0 + 0.01\tau_t$ for Case $\mathrm{Dh_sn1}$. Data samples were collected from the plane $y = 0$. The abscissa and ordinate are normalised by $\omega_{y,\mathrm{rms}}$ the root-mean-square value of ω_y and the mean vapour mass fraction $\langle Y_v\rangle$, respectively. (b) Normalised conditional expectation of the mass fraction of vapour Y_v against the second invariant of the deformation tensor Π_d, which is defined as $\Pi_d = -(S^2 - 1/4\omega_i\omega_i)/2$ [25]. S^2 is the square of the magnitude of the strain rate tensor and ω_i the ith component of vorticity. The high strain rate regions are thus indicated by $\Pi_d < 0$ and high vorticity regions by $\Pi_d > 0$. $\Pi_{d,\mathrm{rms}}$ is the root-mean-square value of Π_d. The thin dotted and dash-dot lines denote Case $\mathrm{Dh_sn1}$ and $\mathrm{Dh_sn2}$, respectively, at $t = t_0 + 0.01\tau_t$; While the thick lines denote the two cases at $t = t_0 + 0.07\tau_t$. The thin dashed and dash-dot-dot lines denote Case $\mathrm{Dh_bn0}$ and $\mathrm{Dh_bn1}$, respectively, at $t = t_0 + 0.07\tau_t$.

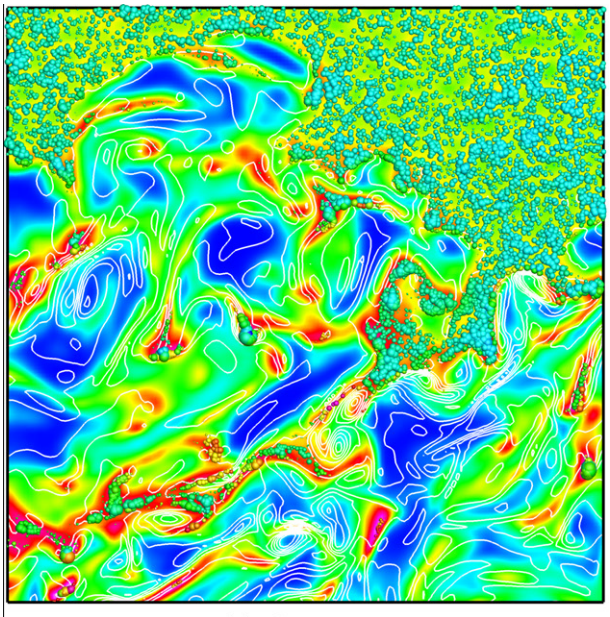

(a) Case Dh_sn1

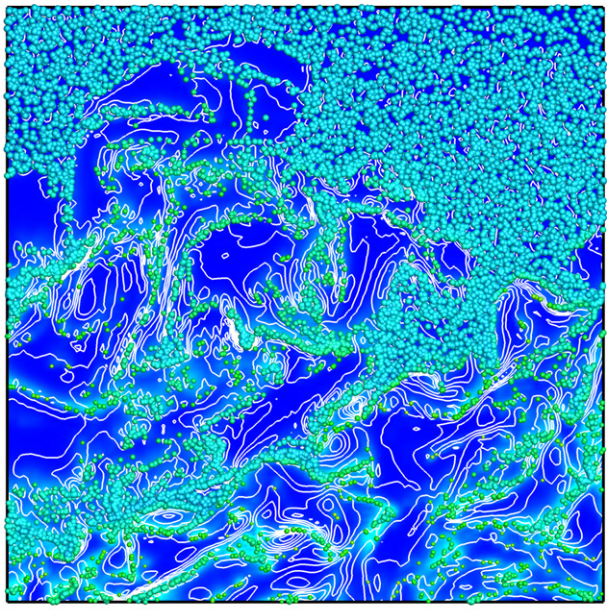

(b) Case Dh_bn0

Fig. 9. Contour plots of the mass fraction of vapour Y_v and spanwise vorticity ω_z superimposed with the instantaneous droplet distribution in a square area $l_x \times l_y = [10,22] \times [0.88,12.88]$ within the plane $z = L_z/2$ for Cases Dh_sn1 and Dh_bn0 at $t = t_0 + 0.07\tau_t$. Y_v is designated by flooded contours and ω_z by white solid lines. Droplets are coloured by the magnitude of the instantaneous evaporation rate $\dot{m}_d$ and sized by mass m_d. Twenty contour levels evenly distributed within the range of $[0,0.50]$ for Y_v, $[-3.27,1.78]$ for ω_z and $[0,1.18 \times 10^{-5}]$ for $|\dot{m}_d|$ are used in both figures. For clarity, the reference length scale used for illustrating droplets in (a) is three times that in (b). (Please note that the initial droplet sizes for the two cases are identical, i.e., $St_0 = 1$.) (For interpretation of the references to colour in this figure legend, the reader is referred to the web version of this article.)

high-strain-rate regions $\Pi_d < 0$ than in high-vorticity regions $\Pi_d > 0$ due to the preferential concentration of droplets in high-strain-rate regions. The overall effect of the smoothing scheme is to decrease the slope of the curves in the high-strain-rate regions and the peak value of the normalised conditional mean vapour mass fraction $\langle Y_v|\Pi_d\rangle/\langle Y_v\rangle$.

It should be pointed out that although the statistics is affected by the fewer data samples available at the two extremes of the range of the sample variable Π_d especially for Cases Dh_bn0 and Dh_bn1 at $t = t_0 + 0.07\tau_t$, the statistics has shown clear trends for the cases studied and the physical mechanisms have been identified.

The above analysis is fully supported by the instantaneous multi-phase flow fields, which are shown in Fig. 9 for Cases Dh_sn1 and Dh_bn0. The contour plots of Y_v and spanwise vorcitiy ω_z are presented together with the instantaneous droplet distribution in a square area $l_x \times l_y = [10,22] \times [0.88,12.88]$ within the plane $z = L_z/2$ at $t = t_0 + 0.07\tau_t$. The instantaneous droplet evaporation rate $\dot{m}_d$ and droplet size m_d are also shown to shed crucial light on the evaporation characteristics for the two cases. Striking difference of how droplets distribute in the turbulent flow can be seen in the two figures. For Case Dh_sn1, droplets are sparsely dispersed in the turbulent mixing layer and almost depleted due to rapid evaporation. Only those accumulated in low vorticity regions can survive. Otherwise, they vanish quickly due to big evaporation rate, as shown in Fig. 9a. In contrast, for Case Dh_bn0, droplets distribute more densely and more uniformly in low vorticity regions, with solitary droplets found here and there. Much less vapour is produced than that for Case Dh_sn1 due to the much larger evaporation time scale $\tau_{v,\infty}$. The vorticity contours are closer to each other and more uneven than in Fig. 9a, designating that more gradients and fluctuations in the vorticity field have been produced by droplets mainly due to the interphase drag in Fig. 9b than those produced by droplets mainly due to evaporation in Fig. 9a at this time. Through comparison, Fig. 9 clearly shows the difference between the droplet dynamic effect and evaporation effect on the turbulent reacting flow.

3.2. $t \in [t_0 + 0.9\tau_t, t_0 + \tau_t]$

The temporal evolution of the integrated TKE across the mixing layer $\int_{x_2} \bar{\rho}_g k dx_2$ is shown in Fig. 10 to demonstrate the inert-droplet and combustion effects on turbulence as the simulation time approaches one turbulent-eddy turn-over time τ_t after the droplet and/or reaction effects are enabled. To facilitate the comparison, the ordinate is normalised by K_0 the integrated TKE at $t = t_0$. It can be seen that all the reacting mixing layers are approaching self-similar state. The integrated TKEs become smaller than the initial value K_0 for all the cases. Different from Fig. 3, the TKEs for Cases Dh_bn0 and Dh_bn1 become the biggest, followed by those for Cases Dh_sn1 and Dh_sn2, and then that for Case RML. Similar to Fig. 3, the integrated TKE shown in Fig. 10 is statistically independent of n_s, i.e., the times of the application of the smoothing scheme to the droplet source terms for droplet cases.

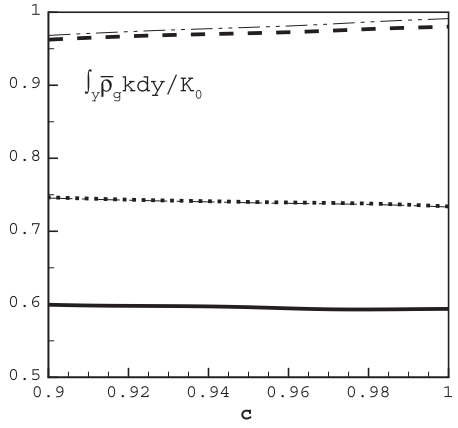

Fig. 10. Temporal evolution of the integrated turbulence kinetic energy in the time period $[t_0 + 0.9\tau_t, t_0 + \tau_t]$. The abscissa denotes the time, i.e., $0.9 \leqslant c \leqslant 1 \Leftrightarrow t_0 + 0.9\text{-}\tau_t \leqslant t \leqslant t_0 + \tau_t$. The ordinate is normalised by K_0 the integrated TKE at $t = t_0$.

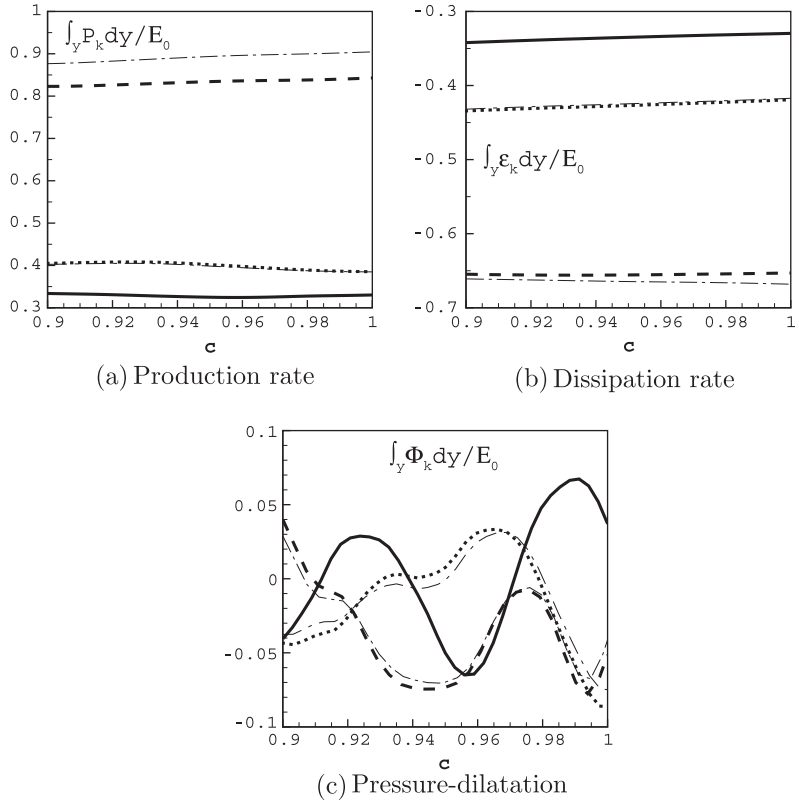

Fig. 11. Temporal evolution of the integrated budget terms in the TKE transport Eq. (20) in the time period $[t_0 + 0.9\tau_t, t_0 + \tau_t]$. The ordinates are normalised by E_0 the magnitude of the integrated turbulence dissipation rate at $t = t_0$.

For Cases RML, Dh_sn1, and Dh_sn2, the magnitude of the integrated turbulence production rate $\int_{x_2} P_k dx_2$ approximately maintains after the heat of combustion is strongly released during $[t_0, t_0 + 0.1\tau_t]$. For Cases Dh_bn0 and Dh_bn1, $\int_{x_2} P_k dx_2$ gradually grows towards the approximately constant value shown in Fig. 11a. The magnitude of the integrated turbulence dissipation rate $\int_{x_2} \epsilon_k dx_2$ slowly decreases towards the approximately constant value shown in Fig. 11b for all the cases. Droplets, especially for Cases Dh_bn0 and Dh_bn1, slow the decrease of $|\int_{x_2} \epsilon_k dx_2|$. Since the magnitude of the integrated dissipation rate (dominant sink) outweighs the integrated production rate (dominant source) for Cases RML, Dh_sn1, and Dh_sn2, the integrated TKE decreases towards the value shown in Fig. 10. While for Cases Dh_bn0 and Dh_bn1, the overturn of magnitude by $\int_{x_2} P_k dx_2$ over $\left|\int_{x_2} \epsilon_k dx_2\right|$ makes the decreased integrated TKE grow again towards the value shown in Fig. 10, which is close to K_0 the initial integrated TKE at $t = t_0$.

To investigate the physical mechanism of the TKE variation, the temporal evolutions of the integrated production, dissipation rates and pressure-dilatation during $[t_0 + 0.9\tau_t, t_0 + \tau_t]$ are shown in Fig. 11. The droplet source terms in Eq. (20) are not presented, since their magnitudes are at least two orders of magnitude smaller than the turbulence production and dissipation rates. The ordinates are normalised by E_0 the magnitude of the integrated turbulence dissipation rate at $t = t_0$. It can be seen that the statistical difference between Case Dh_sn1 and Case Dh_sn2 is negligible, while the difference between Case Dh_bn0 and Case Dh_bn1 for the turbulence production rate $\int_{x_2} P_k dx_2$ is about 7%. Different from Fig. 5c, in which the integrated pressure-dilatation is a dominant term during $[t_0, t_0 + 0.1\tau_t]$, the pressure-dilatation effect shown in Fig. 11c is one order of magnitude smaller than the integrated turbulence production and dissipation rates during $[t_0 + 0.9\tau_t, t_0 + \tau_t]$, as the combustion-released heat decreases and thus the thermal expansion effect diminishes. For all the cases, the integrated pressure-dilatation correlation $\int_{x_2} \Phi_k dx_2$ fluctuates around 0, transferring energy between internal energy and turbulence kinetic energy.

Since the integrated production rate $\int_{x_2} P_k dx_2$ indicates the growth rate (or the time derivative of the momentum thickness) of a temporal mixing layer [20,52], the approximately constant integrated turbulence production rates $\int_{x_2} P_k dx_2$ for all the cases shown in Fig. 11a prove that the droplet-free and droplet-laden reacting mixing layers are approaching their respective self-similarity as the time approaches $t_0 + \tau_t$. For the droplet-free reacting mixing layer case RML, the integrated turbulence production rate approximately balances the integrated turbulence dissipation rate, i.e., $\int_{x_2} P_k dx_2 \approx \int_{x_2} \epsilon_k dx_2$. For Dh_sn1 and Dh_sn2 where the evaporation delay is small, i.e., $\tau_{v,0} \ll \tau_t$, $\int_{x_2} P_k dx_2$ and $\int_{x_2} \epsilon_k dx_2$ are very close to each other. However for Cases Dh_bn0 and Dh_bn1, the magnitude of $\int_{x_2} P_k dx_2$ is bigger than that of $\int_{x_2} \epsilon_k dx_2$, which leads to the integrated TKE slowly increasing (see Fig. 10).

In Fig. 11b, the magnitude of the integrated turbulence dissipation rate $\int_{x_2} \epsilon_k dx_2$ is about 1/3 of E_0 its initial value at $t = t_0$ for Case RML as the interaction time approaches τ_t. The magnitude of $\int_{x_2} \epsilon_k dx_2$ for Cases Dh_sn1 and Dh_sn2 is bigger than that for Case RML. For Cases Dh_bn0 and Dh_bn1, $\left|\int_{x_2} \epsilon_k dx_2\right|$ is close to twice that for Case RML. The physical mechanisms of the increase of turbulence dissipation rate due to droplets have been discussed in Section 3.1, i.e., droplets increase the strain rate magnitude via interphase aerodynamic drag for Cases Dh_bn0 and Dh_bn1 or evaporation for Cases Dh_sn1 and Dh_sn2 due to their preferential concentration in low vorticity, high strain-rate regions. Due to $\tau_{v,\infty} \gg \tau_t$ for Cases Dh_bn0 and Dh_bn1, considerable amount of droplets can still be found in the central region of the turbulent mixing layer as $t \to t_0 + \tau_t$. Therefore the droplet dynamic effect on flow strain continues. As Fig. 12a demonstrates, the integrated squared strain

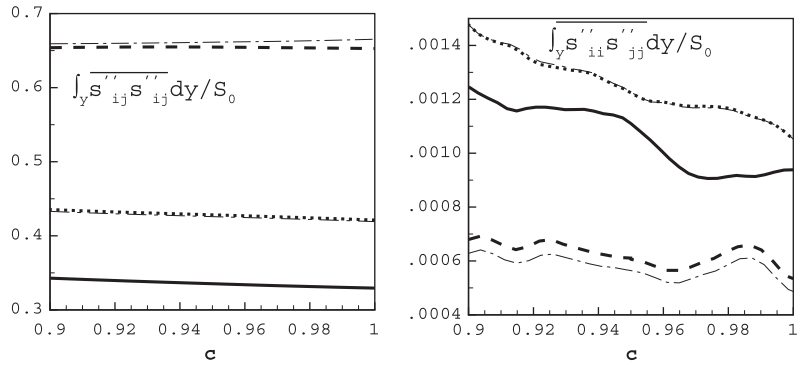

(a) Strain rate (b) Dilatation

Fig. 12. Temporal evolution of the integrated squared strain rate magnitude and squared dilatation magnitude in the time period $[t_0 + 0.9\tau_t, t_0 + \tau_t]$. The ordinates are normalised by S_0 the integrated squared strain rate magnitude at $t = t_0$.

rate magnitude $\int_{x_2} \overline{s''_{ij}s''_{ij}}\,dx_2$ for Cases Dh$_b$n0 and Dh$_b$n1 is close to twice bigger than that for Case RML, similar to the trend discovered in Fig. 11b for $\int_{x_2} \epsilon_k\,dx_2$. For Cases Dh$_s$n1 and Dh$_s$n2, however, droplets are significantly depleted due to the small evaporation delay, i.e., $\tau_{v,0} \ll \tau_t$. Consequently the droplet effects on the strain rate magnitude and TDR are weak, and the magnitudes of $\int_{x_2} \overline{s''_{ij}s''_{ij}}\,dx_2$ and $\int_{x_2} \epsilon_k\,dx_2$ for Cases Dh$_s$n1 and Dh$_s$n2 are only marginally bigger than those for Case RML.

Compared to Fig. 7b in which the integrated squared dilatation magnitude $\int_{x_2} \overline{s''_{ii}s''_{jj}}\,dx_2$ is one order of magnitude smaller than the integrated squared strain rate magnitude $\int_{x_2} \overline{s''_{ij}s''_{ij}}\,dx_2$, $\int_{x_2} \overline{s''_{ii}s''_{jj}}\,dx_2$ is two orders of magnitude smaller than $\int_{x_2} \overline{s''_{ij}s''_{ij}}\,dx_2$ in Fig. 12b, indicating that the compressibility effect due to thermal expansion by combustion is small for all the cases and the TDR is fully determined the strain rate magnitude. It is worth mentioning that different from Fig. 7, the statistics between Case Dh$_s$n1 and Dh$_s$n2, and between Case Dh$_b$n0 and Dh$_b$n1, agrees well with each other in Fig. 12. The impact of the numerical parameter n_s on the statistics of $\int_{x_2} \overline{s''_{ij}s''_{ij}}\,dx_2$ and $\int_{x_2} \epsilon_k\,dx_2$ becomes negligible as $t \to t_0 + \tau_t$.

It then becomes vital to understand the physical mechanism of the variation of the integrated turbulence production rate $\int_{x_2} P_k\,dx_2$, which largely determines the difference of the TKE among the cases as the simulation time approaches one turbulent-eddy turn-over time $t \to t_0 + \tau_t$.

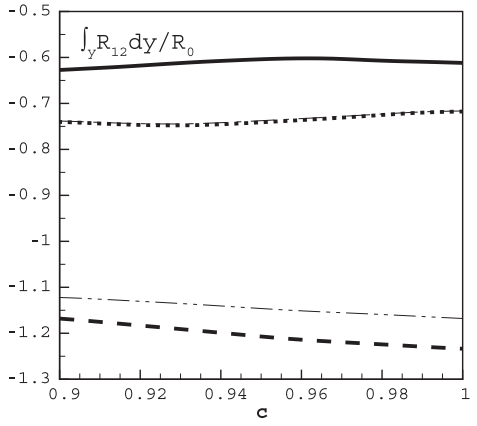

Fig. 13. Temporal evolution of the integrated Reynolds shear stress $\int_{x_2} R_{12}\,dx_2 = \int_{x_2} \overline{\rho_g u''_{g,1}u''_{g,2}}\,dx_2$ in the time period $[t_0 + 0.9\tau_t, t_0 + \tau_t]$. The ordinate is normalised by R_0 the magnitude of the integrated Reynolds shear stress at $t = t_0$, i.e., $R_0 = \left|\int_{x_2} R_{12}\,dx_2\right|_{t=t_0}$.

It is clear that compared to the mean streamwise velocity gradient across the mixing layer $\partial\tilde{u}_{g,1}/\partial x_2$, other mean velocity derivatives can be neglected. As a consequence, the product of the Reynolds shear stress $R_{12} \equiv \overline{\rho_g u''_{g,1}u''_{g,2}}$ and the mean streamwise velocity gradient $\partial\tilde{u}_{g,1}/\partial x_2$ determines the turbulence production rate P_k. It was found that the Reynolds shear stress R_{12} dominates the variation of the turbulence production rate. As shown in Fig. 13, the normalised magnitudes of the integrated Reynolds shear stress $\int_{x_2} R_{12}\,dx_2$ for Cases Dh$_b$n0 and Dh$_b$n1 are considerably bigger, and tend to continuously increase, than those for the droplet-free reacting mixing layer RML and the other two droplet cases Dh$_s$n1 and Dh$_s$n2 in the time period $[t_0 + 0.9\tau_t, t_0 + \tau_t]$. $\left|\int_{x_2} R_{12}\,dx_2\right|$ for Cases Dh$_s$n1 and Dh$_s$n2 is marginally bigger than that for Case RML. For RML, Dh$_s$n1, and Dh$_s$n2, $\left|\int_{x_2} R_{12}\,dx_2\right|$ is smaller than R_0 the magnitude of the integrated Reynolds shear stress at $t = t_0$, i.e., $R_0 = \left|\int_{x_2} R_{12}\,dx_2\right|_{t=t_0}$. While for Cases Dh$_b$n0 and Dh$_b$n1, $\left|\int_{x_2} R_{12}\,dx_2\right| > R_0$ is found in $[t_0 + 0.9\tau_t, t_0 + \tau_t]$.

To detail the analysis of the variation of the Reynolds shear stress R_{12}, the transport equation for the Reynolds stress tensor $\overline{\rho_g u''_{g,i}u''_{g,j}}$ is used. It can be written as follows:

$$\begin{aligned}
&\frac{\partial}{\partial t}\overline{\rho_g u''_{g,i}u''_{g,j}} + \frac{\partial}{\partial x_k}\left(\overline{\rho_g u''_{g,i}u''_{g,j}}\tilde{u}_{g,k}\right)\\
&\quad = -\left(\overline{\rho_g u''_{g,i}u''_{g,k}}\frac{\partial\tilde{u}_{g,j}}{\partial x_k} + \overline{\rho_g u''_{g,j}u''_{g,k}}\frac{\partial\tilde{u}_{g,i}}{\partial x_k}\right) - \frac{\partial}{\partial x_k}\overline{\rho_g u''_{g,i}u''_{g,j}u''_{g,k}}\\
&\quad\quad - \left(\frac{\partial}{\partial x_j}\overline{pu''_{g,i}} + \frac{\partial}{\partial x_i}\overline{pu''_{g,j}}\right) + 2\overline{ps''_{ij}} + \frac{\partial}{\partial x_k}\left(\overline{u''_{g,i}\sigma_{kj}} + \overline{u''_{g,j}\sigma_{ki}}\right)\\
&\quad\quad - \left(\overline{\frac{\partial u''_{g,i}}{\partial x_k}\sigma_{kj}} + \overline{\frac{\partial u''_{g,j}}{\partial x_k}\sigma_{ki}}\right) + \left(\overline{\mathbb{F}_{drag,i}u''_{g,j}} + \overline{\mathbb{F}_{drag,j}u''_{g,i}}\right)\\
&\quad\quad + \left(\overline{\mathbb{E}_{drag,i}u''_{g,j}} + \overline{\mathbb{E}_{drag,j}u''_{g,i}}\right) + \overline{\dot{\mathbb{M}}_d u''_{g,i}u''_{g,j}}.
\end{aligned} \tag{29}$$

The integrated transport equation for the Reynolds stress reads

$$\begin{aligned}
\frac{d}{dt}\int_{x_2} R_{ij}\,dx_2 &= \int_{x_2} P_{ij}\,dx_2 + \int_{x_2} \Phi_{ij}\,dx_2 + \int_{x_2} \epsilon_{ij}\,dx_2 + \int_{x_2} F_{ij}\,dx_2\\
&\quad + \int_{x_2} E_{ij}\,dx_2 + \int_{x_2} M_{ij}\,dx_2,
\end{aligned} \tag{30}$$

where the tensor variables, the Reynolds stress R_{ij}, production rate P_{ij}, pressure-strain Φ_{ij}, dissipation rate ϵ_{ij}, and the droplet source terms F_{ij}, E_{ij}, and M_{ij} are defined as

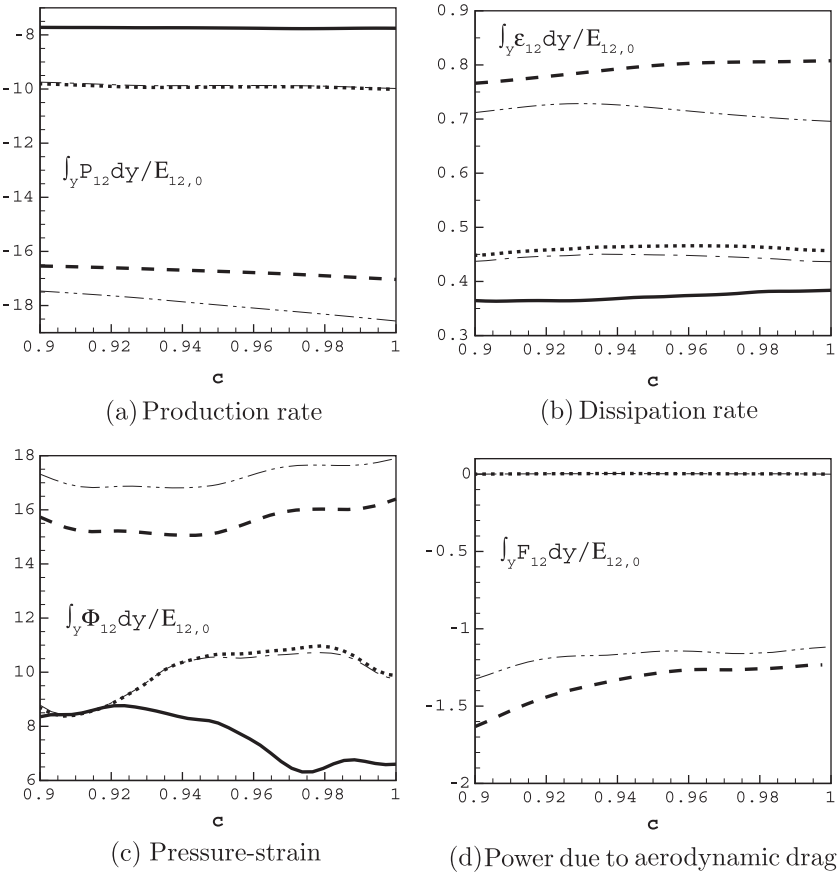

Fig. 14. Temporal evolution of integrated terms in the transport Eq. (30) for the Reynolds shear stress R_{12} in the time period $[t_0 + 0.9\tau_t, t_0 + \tau_t]$. The ordinates are normalised by $E_{12,0}$ the integrated dissipation rate of the Reynolds shear stress at $t = t_0$, i.e., $E_{12.0} = \int_{x_2} \epsilon_{12}\, dx_2|_{t=t_0}$.

$$R_{ij} \equiv \overline{\rho_g u''_{g,i} u''_{g,j}}, \tag{31}$$

$$P_{ij} \equiv -\left(\overline{\rho_g u''_{g,i} u''_{g,k}} \frac{\partial \tilde{u}_{g,j}}{\partial x_k} + \overline{\rho_g u''_{g,j} u''_{g,k}} \frac{\partial \tilde{u}_{g,i}}{\partial x_k}\right), \tag{32}$$

$$\Phi_{ij} \equiv 2\overline{p s''_{ij}}, \tag{33}$$

$$\epsilon_{ij} \equiv -\left(\overline{\frac{\partial u''_{g,i}}{\partial x_k} \sigma_{kj}} + \overline{\frac{\partial u''_{g,j}}{\partial x_k} \sigma_{ki}}\right), \tag{34}$$

$$F_{ij} \equiv \overline{\mathbb{F}_{drag,i} u''_{g,j}} + \overline{\mathbb{F}_{drag,j} u''_{g,i}}, \tag{35}$$

$$E_{ij} \equiv \overline{\mathbb{E}_{drag,i} u''_{g,j}} + \overline{\mathbb{E}_{drag,j} u''_{g,i}}, \tag{36}$$

$$M_{ij} \equiv \overline{\dot{\mathbb{M}}_d u''_{g,i} u''_{g,j}}. \tag{37}$$

Temporal evolution of the integrated shear-stress production rate $\int_{x_2} P_{12}\, dx_2$, dissipation rate $\int_{x_2} \epsilon_{12}\, dx_2$, pressure-strain $\int_{x_2} \Phi_{12}\, dx_2$, and power due to interphase aerodynamic drag $\int_{x_2} F_{12}\, dx_2$ for the integrated Reynolds stress $\int_{x_2} R_{12}\, dx_2$ in the time period $[t_0 + 0.9\tau_t,\ t_0 + \tau_t]$ are shown in Fig. 14. The ordinates are normalised by $E_{12,0}$ the integrated dissipation rate of the Reynolds shear stress at $t = t_0$, i.e., $E_{12.0} = \int_{x_2} \epsilon_{12}\, dx_2|_{t=t_0}$. The other two droplet terms $\int_{x_2} E_{12}\, dx_2$ and $\int_{x_2} M_{12}\, dx_2$ are not shown due to their negligible contributions. Since R_{12} is negative, a source term to R_{12} is negative and a sink term positive. In all the sub-figures, the term magnitudes for Cases $\mathrm{Dh_bn0}$ and $\mathrm{Dh_bn1}$ are considerably bigger than those for Cases $\mathrm{Dh_sn1}$ and $\mathrm{Dh_sn2}$, which are marginally bigger than those for Case RML. It is interesting to note that in Fig. 14, the integrated shear-stress production rate and pressure-strain correlation are the leading source and sink terms, respectively, while $\int_{x_2} F_{12}\, dx_2$ for Cases $\mathrm{Dh_bn0}$, $\mathrm{Dh_bn1}$ and the integrated shear-stress dissipation rate act as source and sink terms, and are one order of magnitude smaller than the respective leading term. The direct droplet effect on flow strain due to the preferential concentration of the $St_0 \approx 1$ droplets, as shown in Figs. 7a and 12a, imposes pivotal consequence on the integrated pressure-strain $\int_{x_2} \Phi_{12}\, dx_2$ for Cases $\mathrm{Dh_bn0}$ and $\mathrm{Dh_bn1}$. In Fig. 14d, $\int_{x_2} F_{12}\, dx_2$ is very close to 0 and thus negligible for Cases $\mathrm{Dh_sn1}$ and $\mathrm{Dh_sn2}$, while for Cases $\mathrm{Dh_bn0}$ and $\mathrm{Dh_bn1}$ the magnitude of $\int_{x_2} F_{12}\, dx_2$ is close to twice the integrated dissipation rate $\int_{x_2} \epsilon_{12}\, dx_2$.

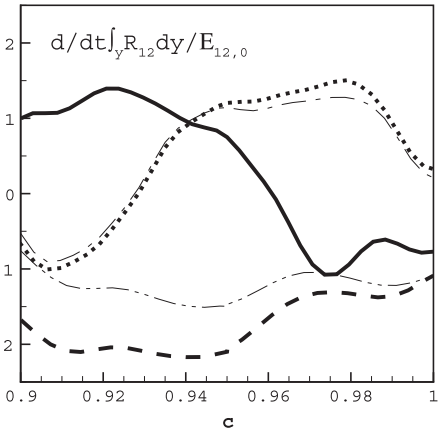

Fig. 15. Temporal evolution of the time derivative of $\int_{x_2} R_{12}\, dx_2$ in the time period $[t_0 + 0.9\tau_t, t_0 + \tau_t]$. It is obtained using $d/dt \int_{x_2} R_{12}\, dx_2 \approx \int_{x_2} (P_{12} + \Phi_{12} + \epsilon_{12} + F_{12}) dx_2$, and normalised by $E_{12,0}$ the integrated dissipation rate of the Reynolds shear stress at $t = t_0$.

To better show the importance of the integrated power term due to the interphase drag $\int_{x_2} F_{12}\,dx_2$, the sums of the four terms shown in Fig. 14 for all the cases are obtained and shown in Fig. 15, after normalised by $E_{12,0}$. It can be seen that for Cases RML, Dh_sn1, and Dh_sn2, the sums fluctuate around 0. The integrated Reynolds shear stresses therefore do not have a mechanism to monotonically increase or decrease, but maintain at a certain level and are approaching their self-similarity (see Fig. 13). For Cases Dh_bn0 and Dh_bn1, it is $\int_{x_2} F_{12}\,dx_2$ which keeps the time derivative $d/dt\int_{x_2} R_{12}\,dx_2$ negative as the time approaches $t_0+\tau_t$. Despite the (acceptable) statistical difference between Case Dh_bn0 and Dh_bn1, it is clear that the magnitude of $d/dt\int_{x_2} R_{12}\,dx_2$ is equivalent to $E_{12,0}$ due to the droplet contribution $\int_{x_2} F_{12}\,dx_2$ during $[t_0+0.9\tau_t, t_0+\tau_t]$. Consequently, the magnitude of $\int_{x_2} R_{12}\,dx_2$ continuously and slowly increases, as shown in Fig. 13.

It now becomes clear that since the droplet evaporation delay $\tau_{v,\infty}$ is big in comparison with the integral turbulence time scale τ_t for Cases Dh_bn0 and Dh_bn1, the droplet dynamic effect due to the aerodynamic drag $\int_{x_2} F_{12}\,dx_2$ plays a vital role in temporal evolution of the integrated Reynolds shear stress $\int_{x_2} R_{12}\,dx_2$, i.e., the increase of its magnitude with time, although $\int_{x_2} F_{12}\,dx_2$ is one order of magnitude smaller than the leading source term-the shear-stress production rate $\int_{x_2} P_{12}\,dx_2$ and the leading sink term-the integrated pressure-strain $\int_{x_2} \Phi_{12}\,dx_2$. The increased magnitude of R_{12} in turn enhances the turbulence production rate P_k, which is determined by the product of the Reynolds shear stress R_{12} and the cross-stream derivative of the mean streamwise velocity $\partial\tilde{u}_{g,1}/\partial x_2$. Continuous increase of the integrated turbulence production rate $\int_{x_2} P_k\,dx_2$ makes its magnitude exceed the integrated turbulence dissipation rate $\int_{x_2} \epsilon_k\,dx_2$ for Cases Dh_bn0 and Dh_bn1, which leads to the integrated TKE considerably bigger than those for the other cases, as shown in Fig. 10. For the droplet cases Dh_sn1 and Dh_sn2 with small evaporation delay ($\tau_{v,0}\ll\tau_t$), there is not a continuous source term for the Reynolds shear stress R_{12}. Therefore the turbulence production and dissipation rates approximately balance each other, which is similar to the scenario for Case RML. The reacting mixing layers thus approach their self-similar states when the simulation time approaches one turbulent-eddy turn-over time τ_t.

The impact of n_s on the statistics has been presented in each figure. It can be seen that there is no statistical difference between Case Dh_sn1 and Case Dh_sn2 in all the figures. For Cases Dh_bn0 and Dh_bn1, the difference is generally more noticeable, but the analysis and findings of the inert-droplet and combustion effects on turbulence in this section are not affected by the discrepancy in statistics. Overall, Fig. 10 shows the difference of $\int_{x_2} K\,dx_2$ between Dh_sn1 and Dh_sn2, and between Dh_bn0 and Dh_bn1, are both negligible after the simulations run over one turbulent-eddy turn-over time τ_t.

4. Summary and conclusions

Direct numerical simulation has been performed to investigate the effects of combustion, droplet evaporation and dynamics on flow turbulence in a diluted diffusion flame through parametric study. To achieve systematic understanding of droplet and combustion effects on turbulence, the analysis is detailed in two time intervals, i.e., $t\in[t_0,t_0+0.1\tau_t]$ immediately after the intense turbulence–combustion–droplets interactions occur at $t=t_0=225$ when a fully turbulent mixing layer has been established, and $t\in[t_0+0.9\tau_t,t_0+\tau_t]$ as the temporally-developing two-phase reacting mixing layers approach self-similarity after the simulations run over one turbulent-eddy turn-over time τ_t.

In $[t_0,t_0+0.1\tau_t]$, the turbulence kinetic energy increases for all the cases. For the droplet cases Dh_bn0 and Dh_bn1 with big latent heat of vaporisation h_{fg}, the TKE is found lower than that in the droplet-free reacting mixing layer RML; While for Cases Dh_sn1 and Dh_sn2 with small h_{fg}, the TKE is higher than that for Case RML. Through the budget analysis of the TKE transport equation, it was found that the predominant contribution comes from the pressure-dilatation effect, which is determined by combustion-released heat. For Cases Dh_bn0 and Dh_bn1, the gas temperature is decreased considerably by the inert droplets through heat exchange to drive evaporation and the pressure-dilatation effect diminished, leading to the lower TKE for the two cases. For Cases Dh_sn1 and Dh_sn2, intense evaporation leads to one of the droplet source terms in the TKE equation, i.e., the additional production rate due to evaporation, predominantly big and on the same magnitude as the pressure-dilatation initially. As a consequence, the TKE becomes the biggest for Dh_sn1 and Dh_sn2 among all the cases.

The turbulence dissipation rate is determined by the squared strain rate magnitude and the squared dilatation magnitude-dilatation dissipation, the former of which is the main contribution to the turbulence dissipation rate for all the cases. The droplets increase the strain rate magnitude mainly due to the evaporation effect for Cases Dh_sn1 and Dh_sn2, where the characteristic evaporation time scale τ_v is small and thus evaporation is rapid, and mainly due to the interphase drag for Cases Dh_bn0 and Dh_bn1, where τ_v is big and thus evaporation is slow. The droplet effects on the turbulence dissipation rate is more profound than the combustion effect due to the preferential concentration of the $St_0=1$ droplets in low vorticity, high strain rate regions, which facilitates the augmentation of the strain rate magnitude through either evaporation or interphase drag and in turn the increase of the magnitude of turbulence dissipation rate. The instantaneous fields of interactions between the turbulent reacting flow and inert evaporating droplets, and the statistics of conditional expectation of the vapour mass fraction Y_v against the second invariant of the deformation tensor Π_d substantiate the analysis.

As the simulation time approaches one turbulent-eddy turnover time τ_t, the integrated TKE for Cases Dh_bn0 and Dh_bn1 becomes the biggest among all the cases, although for all the cases the integrated TKE is lower than the initial value K_0 at $t=t_0$. Among the budget terms in the transport equation of the integrated TKE, the droplet contributions are insignificant, and the integrated pressure-dilatation is one order of magnitude smaller than the integrated turbulence production rate $\int_{x_2} P_k\,dx_2$ and dissipation rate $\int_{x_2} \epsilon_k\,dx_2$ due to diminished combustion-released heat, in contrast to the situation during $[t_0,t_0+0.1\tau_t]$ when combustion-released heat is intense after reaction is initiated. For the droplet-free reacting mixing layer RML and the droplet cases Dh_sn1 and Dh_sn1 with small evaporation delay (and therefore virtually no droplets present in the central region of the turbulent mixing layer), $\int_{x_2} P_k\,dx_2$ and $\int_{x_2} \epsilon_k\,dx_2$ are equivalent or very close to each other in magnitude; While for Cases Dh_bn0 and Dh_bn1, $\int_{x_2} P_k\,dx_2 > \left|\int_{x_2} \epsilon_k\,dx_2\right|$ is found.

The droplet effect on turbulence dissipation rate due to the preferential concentration of the $St\sim 1$ droplets continues for Cases Dh_bn0 and Dh_bn1 due to $\tau_{v,\infty}\gg\tau_t$, while for Cases Dh_sn1 and Dh_sn2 the droplet effect virtually vanishes compared to that in $[t_0,t_0+0.1\tau_t]$, since the vast majority of the droplets has completed evaporation due to $\tau_{v,0}\ll\tau_t$ and vanishes from the central region of the turbulent reacting mixing layer.

From the budget analysis of the transport equation of the integrated Reynolds shear stress $\int_{x_2} R_{12}\,dx_2$, it was found that for Cases Dh_bn0 and Dh_bn1 the integrated power term due to the interphase drag $\int_{x_2} F_{12}\,dx_2$ plays a determining role in enhancing $\int_{x_2} R_{12}\,dx_2$, although its magnitude is smaller than those of the integrated shear-stress production rate $\int_{x_2} P_{12}\,dx_2$ (the leading source) and pressure-strain $\int_{x_2} \Phi_{12}\,dx_2$ (the leading sink) by one order. The increase of the magnitude of $\int_{x_2} R_{12}\,dx_2$ in turn augments the turbu-

lence production rate P_k. Since the integrated turbulence production rate $\int_{x_2} P_k\,dx_2$ exceeds the integrated turbulence dissipation rate $\int_{x_2} \epsilon_k\,dx_2$ in magnitude, the integrated TKE for Cases $\mathrm{Dh_bn0}$ and $\mathrm{Dh_bn1}$ becomes the biggest among all the cases during $[t_0 + 0.9\tau_t, t_0 + \tau_t]$.

Since the hybrid Eulerian–Lagrangian approach is adopted, different methods of distributing droplet source terms onto the Eulerian grids are compared to affirm that the findings in the present study are not dependent on the procedure of source term determination. Specifically, the effect of the times of the application of a smoothing scheme to the droplet source terms S_{ms}, $\overrightarrow{S}_{mo}$, and S_{en} in every time step of DNS, n_s, on the statistics is scrutinised. The numerical parameter n_s practically decides the local Eulerian grid nodes adjacent to a droplet to which the source term is allocated using the conservative smoothing scheme. Overall, for the statistics of the integrated TKE, negligible discrepancy between the droplet cases $\mathrm{Dh_sn1}$ and $\mathrm{Dh_sn2}$, $\mathrm{Dh_bn0}$ and $\mathrm{Dh_bn1}$, is seen in both of the time intervals $[t_0, t_0 + 0.1\tau_t]$ and $[t_0 + 0.9\tau_t, t_0 + \tau_t]$. Statistics of correlations between droplet source term and gas phase flow variables also agrees well between $\mathrm{Dh_sn1}$ and $\mathrm{Dh_sn2}$, $\mathrm{Dh_bn0}$ and $\mathrm{Dh_bn1}$. Notable difference is found for the statistics of the integrated squared strain rate magnitude $\int_{x_2} \overline{s''_{ij} s''_{ij}}\,dx_2$ and integrated turbulence dissipation rate $\int_{x_2} \epsilon_k\,dx_2$ during $[t_0, t_0 + 0.1\tau_t]$ when intense interactions between the turbulent reacting flow and inert evaporating droplets occur. Difference is also found for the statistics of the integrated turbulence production rate $\int_{x_2} P_k\,dx_2$, the integrated Reynolds shear stress $\int_{x_2} R_{12}\,dx_2$, and the budget terms in the transport equation for $\int_{x_2} R_{12}\,dx_2$ between Case $\mathrm{Dh_bn0}$ and $\mathrm{Dh_bn1}$ during $[t_0 + 0.9\tau_t, t_0 + \tau_t]$. All the statistical differences are mainly due to the preferential concentration of the $St \sim 1$ droplets in low vorticity, high strain rate regions. Even so, the statistical difference is acceptable in the way that the analysis and findings in the present study are not affected by the discrepancy.

Concluding the present study, the combustion effect felt by pressure-dilatation at strong exothermicity plays a key role in the variation of TKE. Combustion-released heat also reduces turbulence production rate. Compared to the combustion effect, the droplet effect is secondary, when strong heat is released from combustion, on pressure-dilatation and turbulence production rate. The role of the droplets is to reduce gas temperature via thermal energy exchange between the two phases, and thus reduce the combustion effect on pressure-dilatation and turbulence production rate. For the droplets with small evaporation delay, the droplet effect via the additional production rate due to evaporation competes with pressure-dilatation due to combustion-released heat, and contributes as a dominant source to the variation of TKE. For turbulence dissipation rate that is determined by the strain rate magnitude and dilatation magnitude, droplets have strong effect on strain rate due to the preferential concentration of the droplets in low vorticity, high strain-rate regions, and combustion mainly affects dilatation. For the compressible reacting mixing layer studied in the present study, the dilation magnitude is small compared to the strain rate magnitude even at strong exothermicity. Therefore the droplets take the dominant role in affecting turbulence dissipation rate in comparison with combustion, i.e., largely increasing its magnitude. As the two-phase turbulent reacting mixing layer approaches the self-similarity, reaction is controlled by mixing and combustion-released heat diminished. Droplets with big evaporation delay retain dynamic effects on turbulence dissipation rate. In addition, the mechanical work done by the interphase aerodynamic drag acts as a consistent source to the turbulent shear stress and in turn increases turbulence production rate and TKE.

As summarised, better physical understanding of inert-droplet and combustion effects on turbulence has been achieved using data of DNS of temporally-developing turbulent two-phase reacting mixing layers. It will be valuable information for developing physics-based RANS and LES models for turbulent non-premixed gas combustion diluted with inert droplets. In addition, since distributing source terms of droplets as point sources traced in the Lagrangian framework is a key procedure in the two-way coupling of the mixed Eulerian–Lagrangian approach for simulation and modelling of turbulent multi-phase reacting flow, different source-term-distribution schemes have been compared and decent agreement has been achieved between the cases using different methods. This demonstrates that the numerics is sound and the computer code **MultiPLESTaR** is well developed and implemented, which will be the base for further research on the complex turbulence–combustion–droplets interactions in engineering combustion systems.

Acknowledgments

Financial support from the Brunel Research Initiative & Enterprise Fund (BRIEF) under the Grant No. LBK211 is gratefully acknowledged. Supercomputing resources are from the UK EPSRC Grant No. EP/I000801/1. Special thanks are due to the three anonymous reviewers. Their comments and suggestions have helped significantly improve the quality of the paper.

References

[1] A.H. Lefebvre, G.A. Halls, Proc. Combust. Inst. 7 (1958) 654–658.
[2] A. Krothapalli, L. Venkatakrishnan, L. Lourenco, B. Greska, R. Elavarasan, J. Fluid Mech. 491 (2003) 131–159.
[3] D.L. Daggett, Water Misting and Injection of Commercial Aircraft Engines to Reduce Airport NO_x, Technical Report NASA/CR-2004-212957, NASA Glenn Research Center, 2004.
[4] G. Grant, J. Brenton, D. Drysdale, Prog. Energy Combust. Sci. 26 (2000) 79–130.
[5] P.G. Arias, H.G. Im, P. Narayanan, A. Trouvé, Proc. Combust. Inst. 33 (2011) 2591–2597.
[6] J. Xia, K.H. Luo, H. Zhao, Combust. Sci. Technol. 183 (2011) 487–518.
[7] K.N.C. Bray, Proc. Combust. Inst. 26 (1996) 1–26.
[8] K.N.C. Bray, P.A. Libby, G. Masuya, J.B. Moss, Combust. Sci. Technol. 25 (1981) 127–140.
[9] S.B. Pope, Annu. Rev. Fluid Mech. 19 (1987) 237–270.
[10] T. Poinsot, Proc. Combust. Inst. 26 (1996) 219–232.
[11] R.W. Bilger, Prog. Energy Combust. Sci. 1 (1976) 87–109.
[12] W.P. Jones, in: P.A. Libby, F.A. Williams (Eds.), Turbulent Reacting Flows, Academic Press Ltd., London, 1994, pp. 309–374.
[13] L. Vervisch, T. Poinsot, Annu. Rev. Fluid Mech. 30 (1998) 655–691.
[14] D. Bradley, P.H. Gaskell, X.J. Gu, Combust. Flame 96 (1994) 221–248.
[15] N. Swaminathan, R.W. Bilger, B. Cuenot, Combust. Flame 126 (2001) 1764–1779.
[16] Y.H. Im, K.Y. Huh, S. Nishiki, T. Hasegawa, Combust. Flame 137 (2004) 478–488.
[17] J.Y. Chen, J.E. Lumley, F.C. Gouldin, Proc. Combust. Inst. 21 (1986) 1483–1491.
[18] N. Chakraborty, M. Katragadda, R.S. Cant, Phys. Fluids 23 (2011) [Article No. 07510].
[19] P.A. McMurtry, J.J. Riely, R.W. Metcalfe, J. Fluid Mech. 199 (1989) 297–332.
[20] K.H. Luo, Combust. Flame 119 (1999) 417–435.
[21] S.D. Mason, C.J. Rutland, Proc. Combust. Inst. 28 (2000) 505–513.
[22] D. Livescu, F.A. Jaberi, C.K. Madnia, J. Fluid Mech. 450 (2002) 35–66.
[23] S. Balachandar, J.K. Eaton, Annu. Rev. Fluid Mech. 42 (2010) 111–133.
[24] M.R. Maxey, J. Fluid Mech. 174 (1987) 441–465.
[25] K.D. Squires, J.K. Eaton, Phys. Fluids A 2 (1990) 1191–1203.
[26] S. Elghobashi, G.C. Truesdell, J. Fluid Mech. 242 (1992) 655–700.
[27] J. Réveillon, F.-X. Demoulin, J. Fluid Mech. 583 (2007) 273–302.
[28] F. Mashayek, J. Fluid Mech. 405 (2000) 1–36.
[29] S.V. Apte, K. Mahesh, P. Moin, J.C. Oefelein, Int. J. Multiphase Flow 29 (2003) 1311–1331.
[30] M. Bini, W.P. Jones, J. Fluid Mech. 614 (2008) 207–252.
[31] F.A. Williams, Phys. Fluids 1 (1958) 541–545.
[32] W.P. Jones, C. Lettieri, Phys. Fluids 22 (2010). Article No. 11510.
[33] T. Michioka, R. Kurose, K. Sada, H. Makino, Int. J. Multiphase Flow 31 (2005) 843–866.
[34] Y. Wang, C.J. Rutland, Combust. Flame 149 (2007) 353–365.
[35] N. Patel, S. Menon, Combust. Flame 153 (2008) 228–257.
[36] A. Neophytou, E. Mastorakos, R.S. Cant, Combust. Flame 157 (2010) 1071–1086.
[37] J. Xia, K.H. Luo, Combust. Theory Model. 13 (2009) 901–920.
[38] J.H. Chen, Proc. Combust. Inst. 33 (2011) 99–123.
[39] C.T. Crowe, R. Troutt, J.N. Chung, Annu. Rev. Fluid Mech. 28 (1996) 11–43.
[40] J. Xia, K.H. Luo, S. Kumar, Flow Turbul. Combust. 80 (2008) 133–153.

[41] J. Xia, K.H. Luo, Proc. Combust. Inst. 32 (2009) 2267–2274.
[42] J. Xia, K.H. Luo, Flow Turbul. Combust. 84 (2010) 397–422.
[43] J. Xia, K.H. Luo, Proc. Combust. Inst. 33 (2011) 2581–2590.
[44] R.S. Miller, J. Bellan, J. Fluid Mech. 384 (1999) 293–338.
[45] K.K. Kuo, Principles of Combustion, John Wiley & Sons, New York, 1986.
[46] K.W. Thompson, J. Comput. Phys. 68 (1987) 1–24.
[47] S.K. Lele, J. Comput. Phys. 103 (1992) 16–42.
[48] W. Ling, J.N. Chung, T.R. Troutt, C.T. Crowe, J. Fluid Mech. 358 (1998) 61–85.
[49] A. Ferrante, S. Elghobashi, Phys. Fluids 15 (2003) 315–329.
[50] A.M. Ahmed, S. Elghobashi, Phys. Fluids 12 (2000) 2906–2930.
[51] O. Zeman, Phys. Fluids A 2 (1990) 178–188.
[52] A.W. Vreman, N.D. Sandham, K.H. Luo, J. Fluid Mech. 320 (1996) 235–258.